

AWARD NUMBER: W81XWH-15-1-0021

TITLE: Targeting Neuronal-like Metabolism of Metastatic Tumor Cells as a Novel Therapy for Breast Cancer Brain Metastasis

PRINCIPAL INVESTIGATOR: Siyuan Zhang, M.D., Ph.D.

CONTRACTING ORGANIZATION: University of Notre Dame
Notre Dame, IN 46556

REPORT DATE: May 2018

TYPE OF REPORT: Final

PREPARED FOR: U.S. Army Medical Research and Materiel Command
Fort Detrick, Maryland 21702-5012

DISTRIBUTION STATEMENT: Approved for Public Release;
Distribution Unlimited

The views, opinions and/or findings contained in this report are those of the author(s) and should not be construed as an official Department of the Army position, policy or decision unless so designated by other documentation.

REPORT DOCUMENTATION PAGE

Form Approved
OMB No. 0704-0188

Public reporting burden for this collection of information is estimated to average 1 hour per response, including the time for reviewing instructions, searching existing data sources, gathering and maintaining the data needed, and completing and reviewing this collection of information. Send comments regarding this burden estimate or any other aspect of this collection of information, including suggestions for reducing this burden to Department of Defense, Washington Headquarters Services, Directorate for Information Operations and Reports (0704-0188), 1215 Jefferson Davis Highway, Suite 1204, Arlington, VA 22202-4302. Respondents should be aware that notwithstanding any other provision of law, no person shall be subject to any penalty for failing to comply with a collection of information if it does not display a currently valid OMB control number. **PLEASE DO NOT RETURN YOUR FORM TO THE ABOVE ADDRESS.**

1. REPORT DATE May 2018		2. REPORT TYPE Final		3. DATES COVERED 1 Mar 2015 - 28 Feb 2018	
4. TITLE AND SUBTITLE Targeting Neuronal-like Metabolism of Metastatic Tumor Cells as a Novel Therapy for Breast Cancer Brain Metastasis				5a. CONTRACT NUMBER	
				5b. GRANT NUMBER W81XWH-15-1-0021	
				5c. PROGRAM ELEMENT NUMBER	
6. AUTHOR(S) Siyuan Zhang, E-Mail: szhang8@nd.edu Patricia Schnepf, E-Mail: Patricia.M.Skallos.1@nd.edu				5d. PROJECT NUMBER	
				5e. TASK NUMBER	
				5f. WORK UNIT NUMBER	
7. PERFORMING ORGANIZATION NAME(S) AND ADDRESS(ES) University of Notre Dame, Notre Dame, IN 46556				8. PERFORMING ORGANIZATION REPORT NUMBER	
9. SPONSORING / MONITORING AGENCY NAME(S) AND ADDRESS(ES) U.S. Army Medical Research and Materiel Command Fort Detrick, Maryland 21702-5012				10. SPONSOR/MONITOR'S ACRONYM(S)	
				11. SPONSOR/MONITOR'S REPORT NUMBER(S)	
12. DISTRIBUTION / AVAILABILITY STATEMENT Approved for Public Release; Distribution Unlimited					
13. SUPPLEMENTARY NOTES					
14. ABSTRACT Metastasis is the cause of 90% of all cancer-related deaths with 30% of breast cancer-associated fatalities being attributable to brain metastasis. In this project, we hypothesize that the transcriptome reprogramming of tumor cells through interactions with brain astrocytes reshape metastatic tumor cell metabolism. Here, we report that brain microenvironment epigenetically upregulates glutamate decarboxylase 1 (GAD1) in the tumor cell, a regulator of the GABA neurotransmitter glutamate metabolic pathway, which is critical for brain metastatic outgrowth. Using cell-based co-culture and in vivo brain metastasis imaging models, we found that downregulation of the DNA methyltransferase DNMT1 induced by the brain microenvironment-derived clusterin resulted in decreased GAD1 promoter methylation and subsequent upregulation of GAD1 expression in brain metastatic tumor cells. Most importantly, targeting GABA metabolic pathway using a BBB permeable FDA-approved anti-seizure drug vigabatrin decreased the incidence of brain metastasis in vivo. Taken together, our results show how epigenetic changes in GAD1 expression alter local glutamate metabolism in the brain metastatic microenvironment, contributing to a metabolic adaption that facilitates metastasis outgrowth.					
15. SUBJECT TERMS Cancer metabolism, Brain metastasis, Metastatic outgrowth, Metastatic adaptation, Epigenetic transcriptomal regulation, GABA signaling, Brain intravital imaging, Brain tissue clearing.					
16. SECURITY CLASSIFICATION OF:			17. LIMITATION OF ABSTRACT	18. NUMBER OF PAGES	19a. NAME OF RESPONSIBLE PERSON
a. REPORT	b. ABSTRACT	c. THIS PAGE			USAMRMC
U	U	U	UU	38	19b. TELEPHONE NUMBER (include area code)

Table of Contents

	<u>Page</u>
1. Introduction.....	1
2. Keywords.....	1
3. Accomplishments.....	1
4. Impact.....	5
5.Changes/Problems.....	6
6. Products.....	6
7. Participants & Other Collaborating Organizations.....	7
8. Special Reporting Requirements.....	8
9. Appendices.....	8

1. Introduction.....

Among all breast cancer metastatic relapses, 30% of breast cancer-associated fatalities being attributable to breast cancer brain metastasis. Patients with brain metastatic relapse have a median survival of less than one year. Most of FDA approved therapies have limited blood-brain-barrier (BBB) penetration. As a consequence, metastatic brain environment becomes a sanctuary site for metastatic tumors. Our preliminary data revealed two intriguing phenotypes: 1) robust gliosis (reactive astrocyte) surrounding the brain metastatic tumor cells; 2) neuronal-like transcriptome reprogramming of metabolism genes during the brain metastatic evolution. Based on above observations, we **hypothesize** that neuronal adaptation is critical for the brain metastatic success. As all investigational and FDA-approved neurological drugs targeting neuron-specific receptors penetrate the BBB readily, we reason that clinically available neurological drugs could be repurposed as a novel therapy for breast cancer brain metastasis. Therefore, our overall objective is to explore the functional importance of critical neuronal-like changes during metastatic evolution and target metastatic colonization of the brain with BBB-permeable neurological drugs. We have taken state-of-the-art imaging approaches to study the interaction between the tumor cell and metastatic brain environment. We have also mechanistically determined the functional importance of critical neuronal-like changes during metastatic evolution and target metastatic colonization of the brain with BBB-permeable neurological drugs. In this project, we have proposed two specific aims to explore our hypothesis:

Aim 1: Study the spatial and temporal interactions between brain astrocytes and metastatic tumor cells *in situ*.

Aim 2: Pre-clinically investigate the therapeutic efficacy of co-targeting glutamate receptors signaling and breast cancer driver genes.

2. Keywords.....

Cancer metabolism, Brain metastasis, Metastatic outgrowth, Metastatic adaptation, Epigenetic transcriptional regulation, GABA signaling, Brain intravital imaging, Brain tissue clearing.

3. Accomplishments.....

What were the major goals of the project? What was accomplished under these goals?

In past three years, we have achieved major goals as we have proposed in the SOW. For easy reference, the original Tasks in SOW proposed are listed below as font *italics 11pt*.

Major Task 1 Aim 1.1. Visualize the dynamic interactions between astrocytes and disseminated tumor cells.

Accomplishments: The initial goal of this aim is the using intravital imaging technique to visualize the metastatic seeding and tumor-astrocytes interaction. During the first year of funding, we have perfected the cranial window surgery and intravital imaging technique. We first labeled the blood vessel by i.v. injection of TexasRed-dextran and then measured the average size diameter of the blood vessel that contains tumor cells (Fig. 1a-c). Disseminated tumor cells exhibited a highly diverse morphology and a high degree of membrane deformability

inside the blood vessel. On average, tumor cells colonized in brain microvessels which have vessel diameter between 7.5 -12.5 μm (Fig. 1c). We then established *FVB/N-Tg(GFAP.GFP)^{14Mev/J}* colony from Jax laboratory. In this strain, all astrocytes are genetically labeled with GFP using astrocyte-specific GFAP-promoter. Therefore, it allows us to monitor the dynamic changes of astrocytes using intravital imaging. We have established *GFAP.GFP* mouse colony and performed intravital imaging. After induced mCherry-labeled tumor cells by intracardiac

injection, we collected mouse brain and monitored the GFP-expression in brain astrocytes (Fig. 1d, red: tumor cells, green: astrocytes). We performed ~ 1-hour intravital imaging through the cranial window on Day 0, 1 and 5 days post-injection. We observed a direct interaction

between green astrocyte and red tumor cells (Fig. 1D, day 1 data). In the following larger-scale experiment, we have encountered technical challenges to detect enough tumors that form and outgrow right underneath our cranial imaging window at five days post-injection. As the anatomical location of metastatic seeding is entirely

random, very few cells colonized and can be detected underneath cranial imaging window. After multiple attempts and careful consideration of the risk and potential benefits, we concluded the molecular insights of this imaging experiment are very limited. Although the interactions between astrocyte and tumor were evident, we reasoned that tissue staining based approach could reveal more meaning mechanisms. Therefore, we have since devoted more efforts toward whole tissue clearing based imaging approaches (See below).

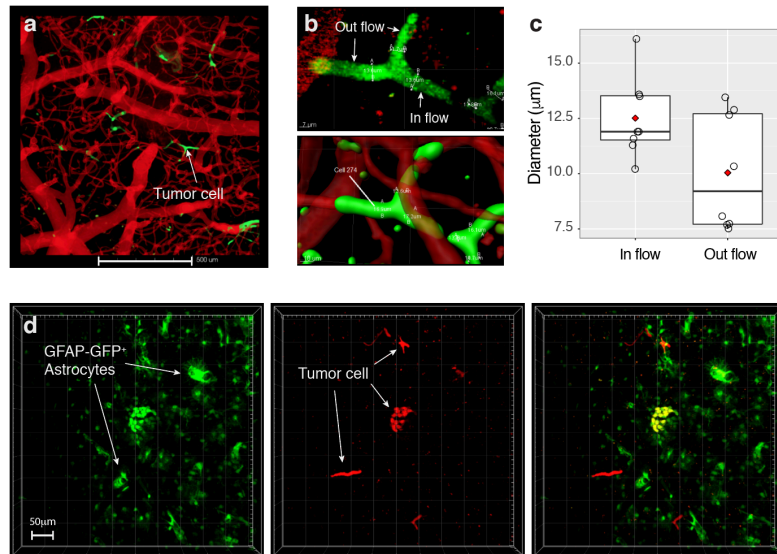


Figure 1 Characterization of intravital imaging of brain metastasis. (a) 3D view of disseminated tumor cell (GFP⁺) and blood vessel staining (TexasRed Dextran). Bar = 500 μm . (b) Measurements of blood vessel confinement of single disseminated tumor cell. Top panel: raw image; bottom panel: 3D reconstructed image. (c) Quantifications of blood vessel confinement. (d) Intravital imaging of metastatic tumor cells in the brain at day 1 of metastasis dissemination. Green: GFAP-GFP⁺ astrocytes; Red: Td-tomato Red labeled tumor cells.

Major Task 2 Aim 1.2: Multiplexed molecular phenotyping of the metabolic and survival signaling of metastatic tumor cells in situ.

Major Task 3 Aim 1.3: Exploring the functional importance of glutamate signaling in early colonization.

Accomplishments: We have made major accomplishment on Aim 1.2 and 1.3. Over the funding period, we were able to adapt whole brain tissue clearing method from the neuroscience field and expand the deep tissue capacity with multiplex immunofluorescence staining. We have achieved whole brain tissue multiplexed staining of astrocyte marker (GFAP), tumor cell marker (cytokeratin 8), blood vessel stain, cell proliferation staining (EdU). We also attempted other antibodies, including neuron marker (NeuN) and Glutamate-receptor genes (GRIA1). Unfortunately, NeuN and GRIA1 antibodies were not compatible with current tissue clearing

methods. We were unable to obtain specific staining. After IF staining of whole tissue, we performed 3D co-registration of multiple metastatic landscape components (tumor cell, blood vessel and astrocytes) with high spatial resolution on a global scale of dimensions up to approximately 4000 um x 4000 um x 3000 um. See Guldner IH et. al. Sci Rep. 2016 in the Appendix for more details.

The vast amount of 3D imaging data also presented a considerable challenge in data analysis. To quantitatively analyze the collaborate with Danny Chen's group at Department of Computer Science and Engineering to further develop the imaging analysis algorithm to unbiasedly analyze the large imaging dataset. We have successfully developed new algorithms and discovered previously underappreciated angiogenesis events during the brain metastasis progression. The fruitful interdisciplinary collaboration has resulted in three publications and three patents disclosures.

Ref:

Yang, L., Zhang, Y., Guldner, I.H. g, **Zhang, S.**, and Chen, D.Z. (2015). Fast Background Removal in 3D Fluorescence Microscopy Images Using One-Class Learning. In Medical Image Computing and Computer-Assisted Intervention – MICCAI 2015, N. Navab, J. Hornegger, W.M. Wells, and A.F. Frangi, eds. (Springer International Publishing), pp. 292–299.

Yang, L., Zhang, Y., Guldner, I.H., **Zhang, S.**, Chen, D.Z. (2016). 3D Segmentation of Glial Cells Using Fully Convolutional Networks and k-Terminal Cut. To be published in Proc. of the 19th International Conference on Medical Image Computing and Computer-Assisted Intervention – MICCAI, October 17-21, 2016.

Guldner, I.H., Yang, L., Cowdrick, K.R., Wang, Q., Alvarez Barrios, W.V. g, Zellmer, V.R., Zhang, Y., Host, M., Liu, F., Chen, D.Z., **Zhang, S.** (2016). An Integrative Platform for Three-dimensional Quantitative Analysis of Spatially Heterogeneous Metastasis Landscapes. Sci Rep. Apr 12;6:24201.

Specific Aim 2 Pre-clinically investigate the therapeutic efficacy of co-targeting glutamate receptors and breast cancer driver genes.

Aim 2.1. Investigate the preclinical efficacy of Talampanel plus Lapatinib combinatorial therapy in the treatment of breast cancer brain metastasis in vitro.

Aim 2.2. Investigate the efficacy of Talampanel plus Lapatinib combinatorial therapy in the prevention of breast cancer brain metastasis in vivo.

Accomplishments:

Our preliminary observation suggested that an up-regulation of glutamate receptor on tumor cells metastasized to the brain. Based on this observation, in the original proposal, we hypothesized that targeting glutamate receptor repurposing brain permeable drug might potentially prevent brain metastasis. We initially proposed to use anti-epilepsy drug Talampanel (INN). Talampanel acts as a non-competitive antagonist of the AMPA receptor, a type of ionotropic glutamate receptor. Talampanel has been clinically tested for treatment of malignant gliomas and amyotrophic lateral sclerosis (ALS). However, after consulting with a neurosurgeon, we realized that the clinical development Talampanel was suspended due to its poor pharmacokinetic profile. Therefore, Talampanel is unlikely to be available in the clinic in the future. Therefore, we decided to search for surrogate target downstream of glutamate signaling.

After further analyze bioinformatics analysis multiple RNA-seq dataset by comparing the transcriptome profile brain metastasis and its primary tumor counterpart, we observed a global down-regulation of the majority of metabolism-related genes in metastatic brain tissues compared with corresponding primary tumors. In contrast, only a small set of metabolism-related genes were up-regulated in brain metastases, suggesting that brain metastases engage a specific metabolic program that is vital for sustaining their energy needs. Through gene set enrichment analysis (GSEA), we further revealed **glutamate decarboxylase 1 (GAD1)** as among the only three significantly up-regulated genes in brain metastases.

GAD1 catalyzes the production of GABA from L-glutamic acid downstream of glutamate receptor. GAD1 is cytosol protein. It facilitates an intracellular GABA metabolism. We reasoned that the GAD1-mediated GABA pathway, downstream of the glutamate receptor, could be the primary method for utilizing glutamine, as an energy source in metastatic tumor cells. To test this hypothesis, we performed GAD1 knockdown experiments under the co-culture of brain microenvironmental cells (primary brain glial cells). Knocking GAD1 significantly abolished tumor cell's survival advantage under glia cell co-culture. We further revealed brain microenvironment-induced downregulation of DNMT1 reactivates GAD1 expression through demethylation of the GAD1 promoter.

We initially proposed to conduct traditional western blot to evaluate the cell signaling events in tumor cells, e.g. MAPK signaling, after perturbation of glutamate pathway. However, the enhanced tumor cell proliferation phenotype requires astrocyte co-culture. The requirement of co-culture made the western blot procedure very cumbersome. We had to separate astrocyte and tumor cells by using FACS sorting before any downstream western blotting. The stressful procedure imposed by FACS sorting largely confounded the metabolic signaling analysis. Therefore, we decided to implement a biosensor based imaging approach to track the glutamate response in situ. We have used an array of biosensors, including NADH-NAD(+) redox sensor, AMPK biosensor, Ca²⁺ signal (pcDN3.1(+)-CaNARi). As shown in the *Schnepp, P.M., et. al. Cancer Res 2017* Fig. 5 (see Appendix), GAD1 mediated a dynamic tumor glutamine metabolic flux and maintains NADH-NAD(+) redox balance under low glucose crisis and blocking GAD1 downstream pathway abolished metastatic tumor outgrowth.

Brain microenvironment-dependent GAD1 upregulation and glutamine metabolism represent a novel therapeutic opportunity for brain metastasis treatment. Modulation of GAD1-mediated GABA metabolism has been clinically exploited previously as anti-epilepsy drug and appeared to be a better strategy than directly target glutamate receptor (like Talampanel does). One such FDA-approved drug, vigabatrin, targets GABA metabolism by inhibiting GABA transaminase (GABA-T), an enzyme directly downstream of GAD1. Vigabatrin thus functions to block GABA flux into the TCA cycle. We examined potential therapeutic effects of vigabatrin for decreasing brain metastatic outgrowth. We further demonstrated that vigabatrin reduced breast tumor cell proliferation in vitro under the astrocyte co-culture. Most importantly, Vigabatrin treatment significantly suppressed brain metastasis formation in two in vivo models supporting the clinical translation/repurposing of FDA approved vigabatrin for brain metastasis treatment. We have reported these significant results in *Schnepp, P.M., et. al. Cancer Res 2017*. Please see appendix for details.

Ref:

Schnepf, P.M., Lee, D.D., Guldner, I.H., O'Tighearnaigh, T.K., Howe, E.N., Palakurthi, B., Eckert, K.E., Toni, T.A., Ashfeld, B.L., and **Zhang, S.** (2017). GAD1 Upregulation Programs Aggressive Features of Cancer Cell Metabolism in the Brain Metastatic Microenvironment. *Cancer Res.* 77, 2844-2856.

Schnepf, P.M., Lee, D.D., Guldner, I.H., O'Tighearnaigh, T.K., Howe, E.N., Palakurthi, B., Eckert, K.E., Toni, T.A., Ashfeld, B.L., and **Zhang, S.** (2017). Brain metastatic microenvironment reshapes cancer cell metabolism through epigenetic up-regulation of glutamate decarboxylase 1. (AACR Scholar-in-Training Award). American Association for Cancer Research Annual Meeting 2017, Washington D.C.

What opportunities for training and professional development has the project provided?

This project provides a unique multidisciplinary training opportunity for trainees who traditionally trained as classic cell/cancer biologists. On the bioengineering side, the whole tissue imaging aspects this project continued to provide unprecedented opportunities for postdoctoral fellows and graduate students to interact with the colleagues in the computer engineering to co-develop novel ways to analyze large biomedical imaging dataset. On the genome biology and bioinformatics side, trainees supported by this project have learned modern bioinformatics tools to analyze microarray/RNA-seq data (both publically available and generated by our lab). The alternative hypothesis (GAD1 mediated glutamate signaling) was a direct result of my graduate student (Schnepf, P.M.)'s careful observations from her bioinformatics analysis. Lastly, from the clinical translational angle, trainees had opportunities to interact with a clinical oncologist and neurosurgeon. Their valuable perspective shaped our study design in targeting GAD1 pathway.

How were the results disseminated to communities of interest?

The research products generated from this project has been presented at the national conferences, including 19th International Conference on Medical Image Computing and Computer-Assisted Intervention, Society of Neuroscience Annual Meeting 2016. An abstract has also been submitted to 2017 AACR meeting. We also routinely participate varies community outreach activities at Notre Dame, e.g. Notre Dame Day and Notre Dame Football Weekend science seminar series, to disseminate our exciting results to lay public. We used our tissue clearing 3D imaging as powerful tools to engage high school students who are interested in STEM career path. For instance, we have hosted an on-site science visit for Penn High School students in the past three years.

What do you plan to do during the next reporting period to accomplish the goals?

Nothing to Report.

4. Impact.....

What was the impact on the development of the principal discipline(s) of the project?

From the technology perspective, we are taking highly innovative imaging approach to study brain metastasis. We are the first group that applies this whole tissue imaging methodology to

study cancer metastasis. As the cancer research shifts from "one-gene a time" approach to a global, unbiased view of cancer as an interconnected tissue, our whole tissue 3D imaging approach provide a unique perspective to traditional cancer research field. From the clinical translational perspective, identify GAD1 is significant. Because repurposing FDA approved BBB-permeable vigabatrin (targeting GAD1 pathway) is a relatively safe metastasis prevention drug and highly clinically translatable. If proven to be successful, similar concepts can be explored for the fast clinical repurposing of other FDA approved drugs for cancer therapy.

What was the impact on other disciplines?

To analyze the big 3D imaging dataset effectively, we have collaborated with colleagues in the computational engineering department who are specialized in imaging progressing to develop robust image segmentation/analysis methods. This productive collaborative effort not only provided biologists a more quantitative way to analysis 3D images but also led to two patent disclosures on the image analysis algorithms.

What was the impact on technology transfer?

Base on the work from this project, we have filed three patent disclosures via Notre Dame Technology Transfer Office:

- 1) Repurposing Current Neurological Drugs for Anti-Metastatic Brain Tumor therapy
Provisional Patent Application: 62/136,705
- 2) A method for fast and accurate removal of background noise in 3D microscopy images
Provisional Patent Application: 62/383,556
- 3) A new method for segmentation of glial cells in 3D microscopy images
Provisional Patent Application: 62/383,556

What was the impact on society beyond science and technology?

Nothing to report

5. Changes/Problems.....

Nothing to report

6. Products.....

Major publications directly related to the field of Cancer Biology:

1. Guldner, I.H., Yang, L., Cowdrick, K.R., Wang, Q., Alvarez Barrios, W.V. g, Zellmer, V.R., Zhang, Y., Host, M., Liu, F., Chen, D.Z., **Zhang, S.** (2016). An Integrative Platform for Three-dimensional Quantitative Analysis of Spatially Heterogeneous Metastasis Landscapes. *Sci Rep.* Apr 12;6:24201.
2. Schnepf, P.M., Lee, D.D., Guldner, I.H., O'Tighearnaigh, T.K., Howe, E.N., Palakurthi, B., Eckert, K.E., Toni, T.A., Ashfeld, B.L., and **Zhang, S.** (2017). GAD1 Upregulation Programs Aggressive Features of Cancer Cell Metabolism in the Brain Metastatic Microenvironment. *Cancer Res.* 77, 2844-2856.

Major meeting abstract:

1. Schnepf, P.M., Lee, D.D., Guldner, I.H., O'Tighearnaigh, T.K., Howe, E.N., Palakurthi, B., Eckert, K.E., Toni, T.A., Ashfeld, B.L., and **Zhang, S.** (2017). Brain metastatic microenvironment reshapes cancer cell metabolism through epigenetic up-regulation of glutamate decarboxylase 1. (AACR Scholar-in-Training Award). American Association for Cancer Research Annual Meeting 2017, Washington D.C.

Publications related to the field of Computational Imaging:

1. Yang, L., Zhang, Y., Guldner, I.H. g, **Zhang, S.**, and Chen, D.Z. (2015). Fast Background Removal in 3D Fluorescence Microscopy Images Using One-Class Learning. In Medical Image Computing and Computer-Assisted Intervention – MICCAI 2015, N. Navab, J. Hornegger, W.M. Wells, and A.F. Frangi, eds. (Springer International Publishing), pp. 292–299.
2. Yang, L., Zhang, Y., Guldner, I.H., **Zhang, S.**, Chen, D.Z. (2016). 3D Segmentation of Glial Cells Using Fully Convolutional Networks and k-Terminal Cut. To be published in Proc. of the 19th International Conference on Medical Image Computing and Computer-Assisted Intervention – MICCAI, October 17-21, 2016.

7. Participants & Other Collaborating Organizations.....

What individuals have worked on the project?

Name:	<i>Siyuan Zhang</i>
Project Role:	<i>PI</i>
Researcher Identifier (e.g. ORCID ID):	<i>A-1276-2014</i>
Nearest person month worked:	<i>3/year</i>
Contribution to Project:	<i>As the PI of this project, Dr. Zhang oversees the project design and data interpretation.</i>
Funding Support:	<i>DoD (this award)</i>

Name:	<i>Patricia Schnepf</i>
Project Role:	<i>Graduate student</i>
Researcher Identifier (e.g. ORCID ID):	<i>NA</i>
Nearest person month worked:	<i>12 month/year</i>
Contribution to Project:	<i>Patricia's thesis work primarily focuses on this project. She plays a major role in conducting in vitro and in vivo biology experiments and bioinformatics analysis.</i>
Funding Support:	<i>Partially funded by DoD (this award) and Walther Foundation for Cancer Research (pre-doctoral fellowship)</i>

Name:	<i>Ian Guldner</i>
Project Role:	<i>Graduate student</i>
Researcher Identifier (e.g. ORCID ID):	<i>NA</i>
Nearest person month worked:	<i>12 months over three years</i>
Contribution to Project:	<i>Ian primarily focuses on developing tissue imaging pipeline and perform imaging data analysis.</i>
Funding Support:	<i>Partially funded by DoD (this award) and departmental teaching assistantship.</i>

Name:	<i>Qingfei Wang</i>
Project Role:	<i>Postdoctoral Fellow</i>
Researcher Identifier (e.g. ORCID ID):	<i>NA</i>
Nearest person month worked:	<i>6 months over three years</i>
Contribution to Project:	<i>Qingfei is responsible for bioinformatics analysis, co-culture experiment, in vivo mouse work.</i>
Funding Support:	<i>Partially funded by DoD (this award) and departmental funds.</i>

Has there been a change in the active other support of the PD/PI(s) or senior/key personnel since the last reporting period?

Nothing to report

What other organizations were involved as partners?

Nothing to report

8. Special Reporting Requirements.....


Nothing to report

9. Appendices.....

Published research papers:

1. Guldner, I.H., Yang, L., Cowdrick, K.R., Wang, Q., Alvarez Barrios, W.V. g, Zellmer, V.R., Zhang, Y., Host, M., Liu, F., Chen, D.Z., **Zhang, S.** (2016). An Integrative Platform for Three-dimensional Quantitative Analysis of Spatially Heterogeneous Metastasis Landscapes. *Sci Rep.* Apr 12;6:24201.
2. Schnepf, P.M., Lee, D.D., Guldner, I.H., O'Tighearnaigh, T.K., Howe, E.N., Palakurthi, B., Eckert, K.E., Toni, T.A., Ashfeld, B.L., and **Zhang, S.** (2017). GAD1 Upregulation Programs Aggressive Features of Cancer Cell Metabolism in the Brain Metastatic Microenvironment. *Cancer Res.* 77, 2844-2856.

SCIENTIFIC REPORTS



OPEN

An Integrative Platform for Three-dimensional Quantitative Analysis of Spatially Heterogeneous Metastasis Landscapes

Received: 13 November 2015

Accepted: 23 March 2016

Published: 12 April 2016

Ian H. Guldner^{1,2,*}, Lin Yang^{3,*}, Kyle R. Cowdrick^{1,2}, Qingfei Wang^{1,2}, Wendy V. Alvarez Barrios^{1,2}, Victoria R. Zellmer^{1,2}, Yizhe Zhang³, Misha Host^{1,2}, Fang Liu^{2,4}, Danny Z. Chen^{2,3} & Siyuan Zhang^{1,2}

Metastatic microenvironments are spatially and compositionally heterogeneous. This seemingly stochastic heterogeneity provides researchers great challenges in elucidating factors that determine metastatic outgrowth. Herein, we develop and implement an integrative platform that will enable researchers to obtain novel insights from intricate metastatic landscapes. Our two-segment platform begins with whole tissue clearing, staining, and imaging to globally delineate metastatic landscape heterogeneity with spatial and molecular resolution. The second segment of our platform applies our custom-developed SMART 3D (Spatial filtering-based background removal and Multi-channel forest classifiers-based 3D ReconsTruction), a multi-faceted image analysis pipeline, permitting quantitative interrogation of functional implications of heterogeneous metastatic landscape constituents, from subcellular features to multicellular structures, within our large three-dimensional (3D) image datasets. Coupling whole tissue imaging of brain metastasis animal models with SMART 3D, we demonstrate the capability of our integrative pipeline to reveal and quantify volumetric and spatial aspects of brain metastasis landscapes, including diverse tumor morphology, heterogeneous proliferative indices, metastasis-associated astrogliosis, and vasculature spatial distribution. Collectively, our study demonstrates the utility of our novel integrative platform to reveal and quantify the global spatial and volumetric characteristics of the 3D metastatic landscape with unparalleled accuracy, opening new opportunities for unbiased investigation of novel biological phenomena *in situ*.

Tumor metastasis is orchestrated by the interplay between genetically heterogeneous cancer cells and a spatially and compositionally heterogeneous tumor microenvironment (TME, also referred to as the metastatic niche)^{1–5}. Metastatic cells and the metastatic TME – together, termed the metastatic landscape – are composed of several different cell types that display an ever-evolving heterogeneity throughout metastatic progression^{6–8}. It has been envisioned that spatially compartmentalized metastatic niches differentially regulate metastatic progression^{6–8}. For example, the role of astrogliosis during brain metastasis formation has been debated for decades^{9,10}. Limited by two-dimensional (2D) *in vitro* culture and histology methods, previous studies were unable to fully describe the spatial heterogeneity of astrogliosis or deduce the functional implications of astrogliosis during brain metastasis progression *in situ* within large, intact tissue samples. Similarly, angiogenesis, a hallmark of cancer, is crucial to maintain brain tumor outgrowth, such as in gliomas^{1,11}. Yet, the requirement and characterization of angiogenesis during brain metastasis progression remain largely controversial¹⁰. Because only a small fraction of the total vasculature can be captured in a single standard histological slice, even the most concrete brain metastasis vascularisation data draw speculative conclusions. Despite the significance of examining spatial aspects of

¹Department of Biological Sciences, College of Science, University of Notre Dame, Notre Dame, IN 46556, USA.

²Mike and Josie Harper Cancer Research Institute, University of Notre Dame, 1234 N. Notre Dame Avenue, South Bend, IN 46617, USA. ³Department of Computer Science and Engineering, College of Engineering, University of Notre Dame, Notre Dame, IN 46556, USA. ⁴Department of Applied and Computational Mathematics and Statistics, College of Science, University of Notre Dame, Notre Dame, IN 46556, USA. *These authors contributed equally to this work. Correspondence and requests for materials should be addressed to S.Z. (email: szhang8@nd.edu)

heterogeneous metastases in their metastatic niche, technical barriers have impeded efforts to dissect the contribution of diverse spatial components of the metastatic landscape *in situ* on a global three-dimensional (3D) scale with molecular-level resolution¹².

The recent boom of whole tissue clearing techniques presents us with an unprecedented opportunity to dissect metastatic heterogeneity *in situ*¹³. Tissue clearing permits a holistic, 3D view of tissue, which is particularly useful to image two metastatic landscape components – astrocytes and vasculature – that cannot be captured in a single plane and have diverse or highly speculated roles in metastatic progression^{9,10,14–16}. Furthermore, the 3D perspective provided by tissue clearing allows spatial analysis, which can provide novel insights into biological phenomena. While tissue clearing provides an unmatched opportunity to explore the metastatic landscape, the massive volumetric datasets derived from whole tissue imaging impose new challenges on the image analysis of multiple genetic events with statistically significant biological implications. In this study, we developed and applied an integrative platform including a 3D whole brain imaging approach, consisting of whole tissue clearing, staining, and imaging, followed by customized computer-assisted quantifications. We developed SMART 3D (Spatial filtering-based background removal and Multi-channel forest classifiers-based 3D ReconsTruction), a multi-faceted image analysis pipeline, to observe and quantify phenotypic metastatic landscape heterogeneity *in situ* with spatial and molecular resolution. Our implementation of our integrative platform to globally analyze the heterogeneous metastasis landscape of brain metastases demonstrates the feasibility of quantitative, multiplexed 3D analysis *in situ* from the molecular level to the whole organ scale. Furthermore, our study asserts the promise of such analysis in revealing unique spatial patterns of metastasis that will lead to novel functional and molecular insights into the dynamic nature of metastasis.

Results

Global imaging of multiple metastatic landscape features with molecular resolution. We streamlined a whole tissue clearing, staining, imaging, and computation analysis^{17,18} pipeline to quantitatively analyze and thereby enable the elucidation of the functional impact of phenotypic heterogeneity of the metastatic landscape on metastatic outgrowth (Fig. 1a, Supplementary Fig. S1a). The first segment of our pipeline (Fig. 1a, top), consisting of whole tissue clearing, staining, and imaging, ultimately conquers the long-standing challenge of capturing multiple genetic events in their native 3D context *in situ* to allow a holistic view of the tissue and its compositional and spatial heterogeneity. Tissue clearing and refractive index matching rendered the brain lipid-free and optically transparent, allowing for thorough multiplexed molecular phenotyping of large tissue sections (Supplementary Fig. S1b,c and Supplementary Video S1). Further, cleared brain tissue permitted an approximate five-fold increase in imaging depth from ~500 μm (Fig. 1b, left) to ~3000 μm (Fig. 1b, right). Distinguished from previous tissue clearing-based studies, which primarily relied on transgenic mice that express fluorescent proteins, our approach relied on multiplexed staining for proliferative nuclei, metastatic tumor cells, and TME components (e.g., astrocytes), allowing 3D co-registration of multiple metastatic landscape components with high spatial resolution on a global scale of dimensions up to approximately 4000 $\mu\text{m} \times 4000 \mu\text{m} \times 3000 \mu\text{m}$ (Fig. 1c and Supplementary Video S2). This exponential increase of data content enabled us to reconstruct the brain metastasis landscape in 3D, providing new, exceptionally accurate perspectives on phenotypic heterogeneity, such as the highly irregular tumor morphology that is masked in two-dimensional images (Fig. 1d). We were able to glean detailed information from large, continuous tissue structures, such as blood vessels (Supplementary Fig. S1d), while maintaining high 3D resolution at the cellular level, such as one single extravasated metastatic cell (Fig. 1e), and subcellular details, such as dividing nuclei (Fig. 1f).

Spatial background removal and forest classifiers-based multi-channel 3D reconstruction (SMART 3D: Spatial Multi-channel Reconstruction 3D). Accurate image segmentation is a prerequisite for quantitative analysis of the spatial relationship between metastatic cells and the metastatic niche. The second and third segments of our integrative pipeline (Fig. 1a, bottom) tackle both the extensive problems (e.g., background removal, multi-channel reconstruction) faced in processing large 3D datasets with multiple channels as discussed in detail below. Despite a significant increase of 3D imaging depth enabled by tissue clearing, strong auto-fluorescence background (noise signal) and inhomogeneous fluorescent staining across the whole tissue significantly limit the applicability of existing 2D computational algorithms for accurate segmentation and visualization of large, multi-channel volumetric 3D datasets. Thus, the first step of our image analysis aimed to remove the background noise in the 3D datasets.

We developed a new approach that combines the spatial filtering method and optimization-based methods for this background removal problem on 3D images¹⁹. Due to wide variations in the sizes of foreground objects in 3D datasets, it is very difficult to select one single appropriate window size or ball size for the spatial filtering method and the rolling ball algorithm²⁰. We applied percentile filtering with a window size that is slightly larger than the size of the smallest object (e.g., the size of a cell) in the image to estimate a rough background. Subsequently, we used unsupervised one-class learning²¹ to detect errors in this rough estimation (Fig. 2a). Finally, these errors were corrected in the re-estimation process and the refined background estimation was obtained for generating a noise-reduced image. The processing speed of our new background removal method¹⁹ is comparable to the rolling ball algorithm²⁰ (~30 hours on a Xenon CPU E5-2660v3 for processing a 512 \times 512 dataset). This novel algorithm yields the unprecedented efficiency in removing background while preserving fine structural details (e.g., fine processes of astrocytes) (Fig. 2a, bottom panel).

To compute voxel-level image segmentation with high tolerance of inhomogeneous fluorescent staining, we extracted feature vectors representing each voxel's appearance and texture from multiple channels and concatenated the feature vectors from different channels into a multi-channel feature vector (MFV) (Fig. 2b). Next, we formulated the voxel-level segmentation problem as a classification problem (Fig. 2c). Several classifiers were trained to determine whether a voxel belongs to a specific type of foreground (e.g., tumor cells, astrocytes, blood

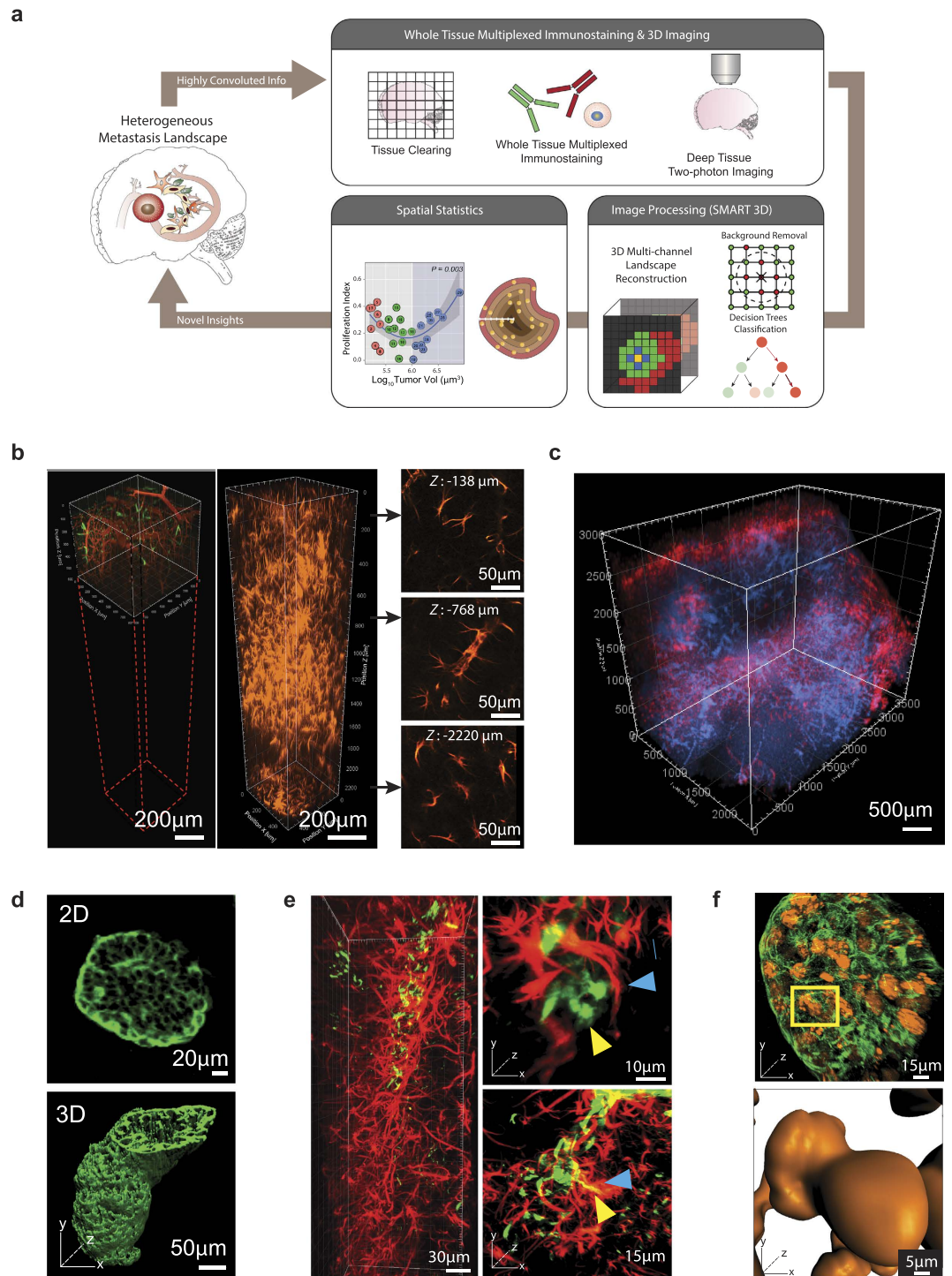


Figure 1. 3D Whole Tissue Imaging of the Brain Metastasis Landscape with Molecular Resolution.

(a) Schematic of our integrative platform consisting of whole tissue clearing, staining, and imaging and SMART 3D (image processing and quantification). (b) Comparison of multiphoton-imaging depth without (left) or with (right) optical tissue clearing. 2D slices are extracted from indicated depths in the tissue-cleared z-stack to demonstrate image quality at various imaging depths. (c) Multiphoton image of 3D global view ($2500 \mu\text{m} \times 3500 \mu\text{m} \times 3000 \mu\text{m}$) of optically cleared mouse brain with multiple MDA-MB-231.Br-derived metastases. Red: anti-GFAP; blue: DAPI. (d) 2D multiphoton image (top) and 3D surface generated image (bottom) of PNA.Met1 brain metastases stained with anti-cytokeratin 8 (K8). (e) 3D multiphoton image of astrocytes (GFAP, red) of the blood brain barrier (left) and astrocyte interaction with MDA-MD-231.Br metastatic cells (right). Blue arrows point to astrocytes, and yellow arrows point to metastatic cells. (f) 3D multiphoton image of PNA.Met1 brain metastasis (K8, green) and EdU-tagged nuclei (orange) (top) and enlarged view of dividing nuclei (bottom).

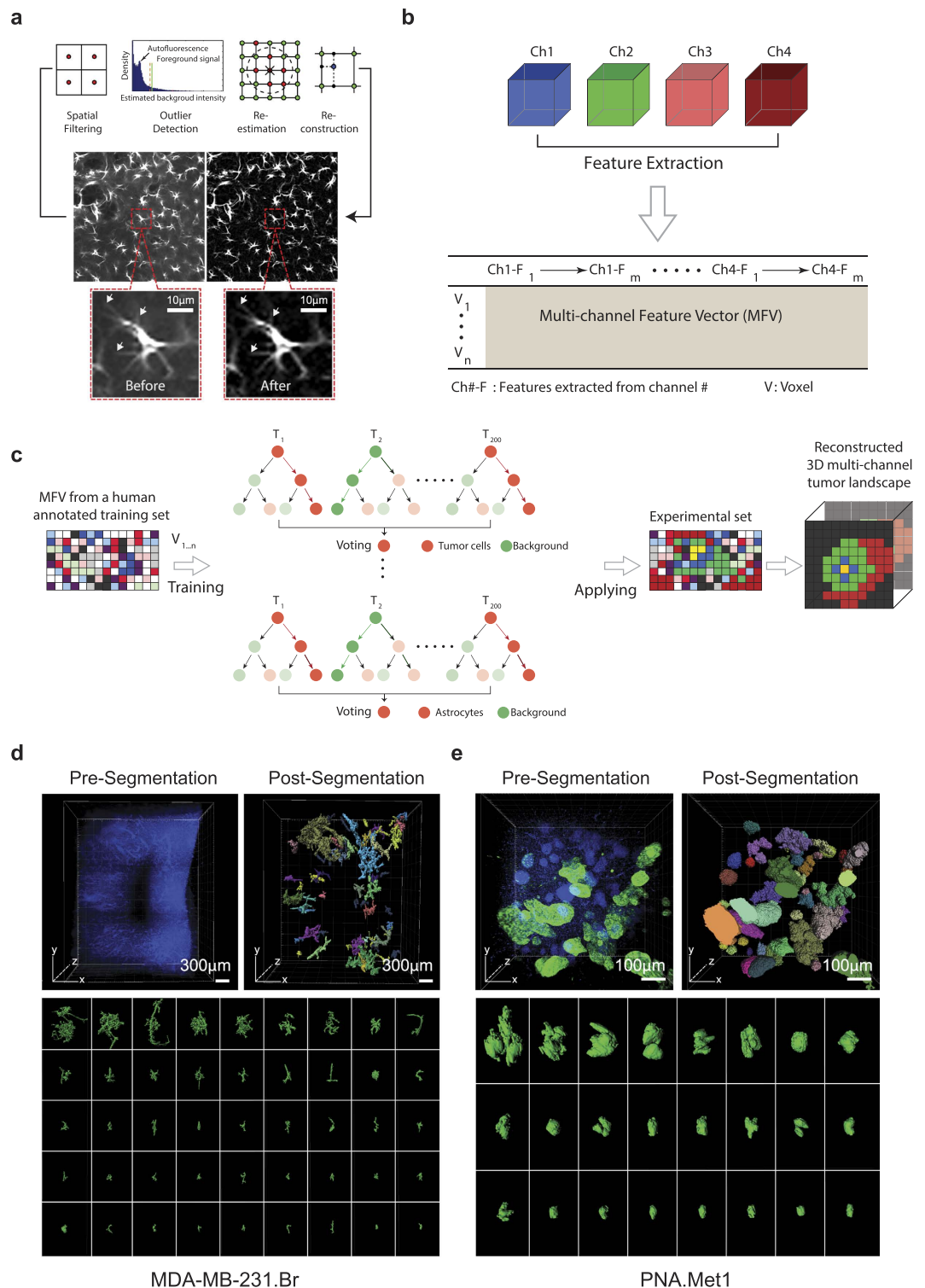


Figure 2. Spatial Filtering-Based Background Removal and Multi-Channel Forest Classifiers-Based 3D (SMART 3D) Reconstruction of Metastatic Heterogeneity. (a) Schematic of the background removal process. Arrow points to fine astrocyte processes preserved by this method. (b) Schematic of multi-channel feature extraction. (c) Schematic of the process of voxel-level segmentation based on random forest classification. (d) Image of DAPI stained MDA-MB-231.Br brain metastases sample before (top left) and after (top right) DAPI cluster-based tumor segmentation and surface generation. Color codes represent individually identified tumors. Bottom panel: whole spectrum of individual morphologically heterogeneous tumors. (e) Image of DAPI (blue) and K8 (green) stained PNA.Met1 brain metastases before (top left) and after (top right) K8/DAPI-based segmentation and surface generation. Bottom panel: whole spectrum of individual morphologically heterogeneous tumors.

vessels, etc.) or the background based on MFV. These classifiers (200 trees and 2 candidate features in each node) were then applied to every voxel in the 3D volumetric datasets to generate the segmentation of desired features (Fig. 2c). To test the accuracy of the classifier, we manually labeled 10 slices for each different component (e.g., tumor, astrocyte, EdU proliferation marker, and blood vessel) and used labeled features as the ground truth. The accuracy was then measured by the F1 score of 10-fold cross validation. F1 score is the harmonic mean of precision and recall, and it is a widely used measure to evaluate the performance of the classifier²². According to the F1 score evaluation, volume quantification errors are approximately $-3.35%$, $-0.03%$, $+8.51%$, $+1.86%$ for tumors, astrocytes, proliferating cells, and blood vessels, respectively (Supplementary Table S1). Finally, we applied the SMART 3D pipeline to a series of 3D multi-channel datasets to reconstruct and quantify the metastasis landscape (Figs 2d and 3–5).

Heterogeneous morphology of breast cancer brain metastases. To test the robustness of SMART 3D, we generated experimental brain metastases using two breast cancer brain metastasis models with distinct morphologies: MDA-MB-231.brain-seeking (Br) human breast cancer cells in an immunocompromised (Rag1 $-/-$) mouse and PNA.Met1 murine breast carcinoma cells in an FVB host. We stained metastasis-burdened samples with the epithelial cell-specific marker cytokeratin 8 (K8) antibody to identify breast cancer brain metastases, as K8 is absent in normal cerebral cortex (Supplementary Fig. S2a). In addition, tumor cell nuclei displayed unique pleomorphism distinct from neural tissue nuclei, allowing for further nuclear-based tumor cell identification. Our SMART 3D algorithm was adaptive to diverse tumor morphologies in 2D and 3D (Supplementary Fig. S2b,c) and proved to be robust as indicated by the overlap between the original 3D images and the computationally segmented voxels (Supplementary Fig. S2d). Surface renderings of the SMART 3D-segmented metastases within the same metastatic niche revealed a previously underappreciated array of morphological heterogeneity (Fig. 2d,e). The MDA-MB-231.Br metastases are highly branched, reflecting their exclusive growth along brain vasculature (vessel co-option)²³, whereas PNA.Met1 metastases form irregularly shaped clusters (Supplementary Video S3), reflecting the morphology of brain metastases observed in the clinic. Within the same metastatic niche, the volumes of metastatic tumors are extremely diverse, ranging from $9.6\text{--}857.7 \times 10^3 \mu\text{m}^3$ to $155.3\text{--}8074.0 \times 10^3 \mu\text{m}^3$ for MDA-MB-231.Br and PNA.Met1 tumors, respectively. This broad spectrum of metastasis volumes suggested a wide range of developmental stages of metastatic lesions within the same TME.

Metastasis developmental stage shapes a non-linear proliferative heterogeneity. Taking advantage of the multi-channel spatial segmentation and quantification capacities of SMART 3D, we next surveyed the proliferation status of every tumor cell in each metastasis by 5-ethynyl-2'-deoxyuridine (EdU) detection²⁴. Both metastasis models displayed a wide spectrum of proliferative indices, from less than 1% to as much as 56%. Interestingly, metastases of similar sizes had very disparate proliferative indices (Fig. 3a,b). Kernel density estimation (KDE, “Gaussian”) for MDA-MB-231.Br metastases showed that small and medium metastases had a wide range of proliferation scattered across proliferative indices (0–0.3) and large metastases had a relatively uniform level of proliferation concentrated between 0.1 and 0.2 proliferative indices. The difference between the variance of proliferation between large metastases (Log_{10} tumor volume > 5.0) and small and medium metastases are statistically significant ($p = 0.012$, F-test) (Fig. 3c). KDE (“Gaussian”) for PNA.Met1 metastases revealed a different pattern of proliferation, with a wide range of heterogeneity for small and large metastases, but a narrower range of proliferation for medium metastases primarily concentrated at 0.2 proliferative index (Fig. 3d, left). Interestingly, a parabola-shaped trend ($p = 0.003$, quadratic regression) fit the data of tumor proliferative index versus metastasis volume, in which the vertex of the parabola was within the medium-sized metastasis range and approached a proliferative index of 0.15. Notably, two tumors (i.e., tumors 14 and 19) fell below the vertex and had negligible proliferation (Fig. 3d, right).

Leveraging the spatial aspect of our 3D imaging approach, we next probed the spatial distribution of proliferative cells within metastases. We did so by performing concentric zone analysis in which we analyzed the proliferative indices of concentric 10 μm -thick volumetric zones from the tumor surface to the tumor core (Fig. 3e). Linear regression analysis demonstrated distinct proliferative kinetics in which small tumors have a sharp proliferative index drop-off approaching the tumor core (proliferative index drops from ~ 0.5 to 0.12, $p < 0.001$), while the tumor core remains proliferative in medium and large sized tumors (Fig. 3f). Notably, there is extensive proliferative heterogeneity both among individual metastases and the zones within individual metastases (Fig. 3g). Even similarly sized tumors have dramatically different maximum proliferative indices (e.g., tumors 18 and 19) and proliferative patterns among zones from the surface to the core (e.g., tumors 16–18).

Metastasis-induced astrogliosis influences proliferative heterogeneity of tumors. In his “seed and soil” hypothesis, Stephen Paget first proposed that the tumor microenvironment is both essential and important in metastatic seeding and outgrowth²⁵. To explore microenvironmental factors that potentially influence metastatic outgrowth while taking advantage of the holistic view provided by 3D imaging, we first examined the astroglial response to brain metastases, a response that 2D imaging insufficiently captures in terms of astrocyte morphology and spatial distribution (Supplementary Fig. S3). Previous studies have suggested that the astroglial response promotes metastatic outgrowth^{26–33}. To accurately characterize the astrocyte response to brain metastases, we imaged the astroglial response in 3D to obtain complete astrocyte morphology in exquisite detail (Supplementary Fig. S3) and further applied SMART 3D to clearly distinguish anti-GFAP staining from background noise in 2D and 3D (Supplementary Fig. S3). This enabled us to reconstruct and quantitatively analyze spatial astrogliosis patterns on a global scale (Fig. 4a). Qualitative analysis of astrogliosis revealed that astrocyte coverage of tumors was not spatially uniform around metastases and the volume of astrogliosis was variable among metastases in both the PNA.Met1 model (Fig. 4b) and the MDA-MB-231.Br model (Supplementary Fig. S4). Notably, the early astroglial response (gliosis index) appeared to be negatively correlated with metastasis

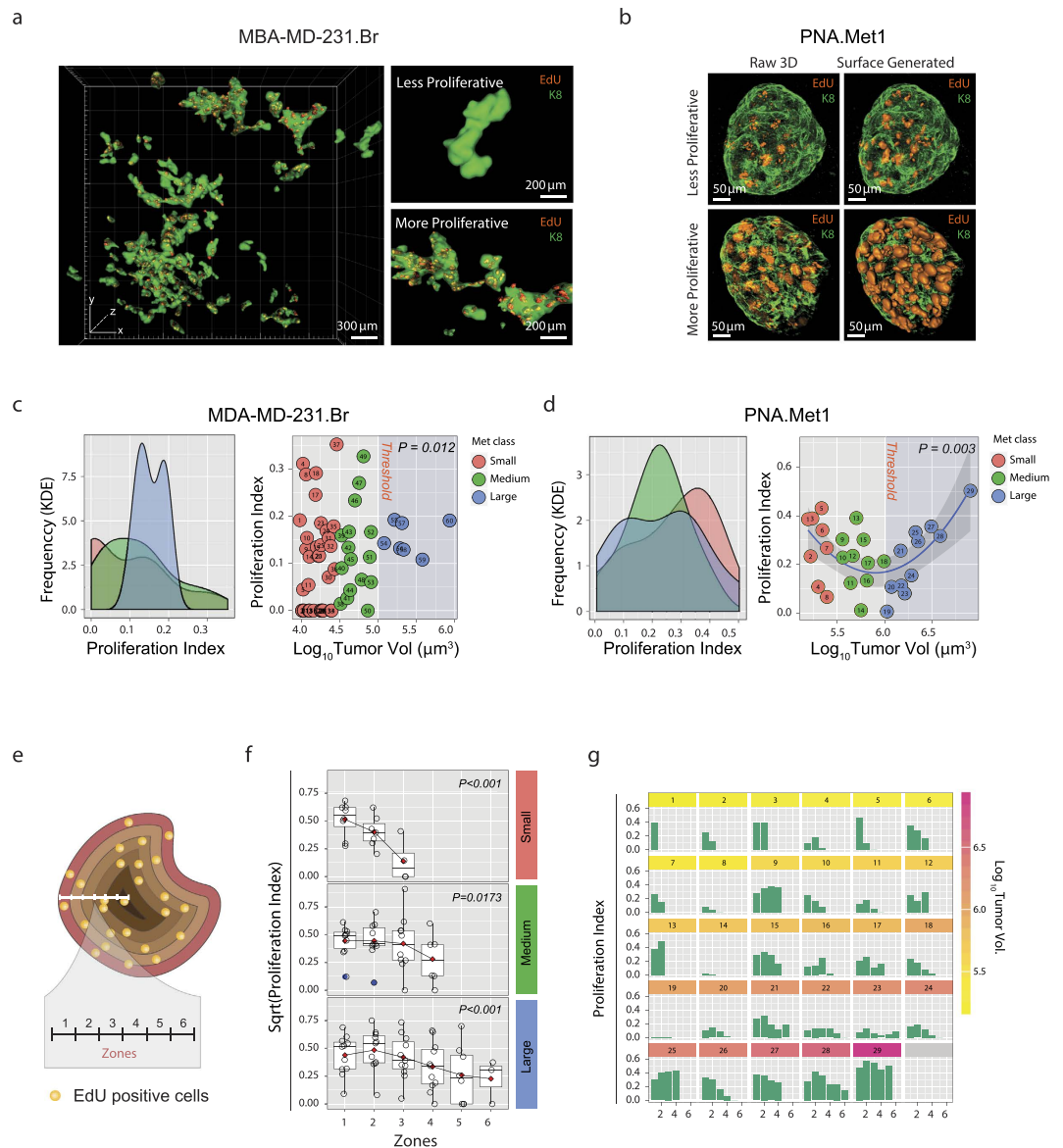


Figure 3. Proliferative Heterogeneity in PNA.Met1 and MDA-MB-231.Br Breast Cancer Brain Metastases.

(a) Global 3D surface rendering of multiphoton images of MDA-MB-231.Br brain metastases (green) and EdU-tagged nuclei (orange) demonstrating proliferative heterogeneity within the same anatomical region (left) from low proliferation (top right) to high proliferation (bottom right). (b) 3D multiphoton images (top) and associated surface generated images (bottom) focusing on EdU-tagged nuclei (orange) in representative less proliferative (left) and more proliferative (right) PNA.Met1 metastases (K8, green). (c) Kernel density estimation (KDE) plot of the proliferative indices of small, medium, and large MDA-MB-231.Br metastases (left) and plot of the relationship between the proliferative index and the \log_{10} of the tumor volume of each MDA-MB-231.Br metastasis (right). Proliferative index = Total EdU voxel volume/Total tumor voxel volume. (d) Kernel density estimation plot of the proliferative indices of small, medium, and large PNA.Met1 metastases (left) and quadratic regression plot of the relationship between the proliferative index and the \log_{10} of the tumor volume of each PNA.Met1 metastasis (right). Proliferative index is defined as panel C. (e) Schematic representation of concentric zone analysis to analyze spatial characteristics of metastatic proliferation. Zone depth = 10 μm . (f) Regression analyses of the proliferative indices among zones of small (top), medium (middle), and large (bottom) PNA.Met1 brain metastases. Red diamond = mean of each group. P value is based on linear regression model. (g) Bar graphs of the proliferative index within each 10 μm zone for each PNA.Met1 brain metastasis.

proliferation ($r = 0.648$) (Fig. 4d). When metastatic outgrowth progressed, the level of astrogliosis was positively correlated with the proliferation indices of metastases in both medium ($r = 0.700$) and large ($r = 0.656$) tumor groups (Fig. 4d,e). Interestingly, two medium to large-sized metastases (i.e., tumors 14 and 19) have negligible gliosis, and also have extremely low proliferative indices. Importantly, tumor 19, which had no associated

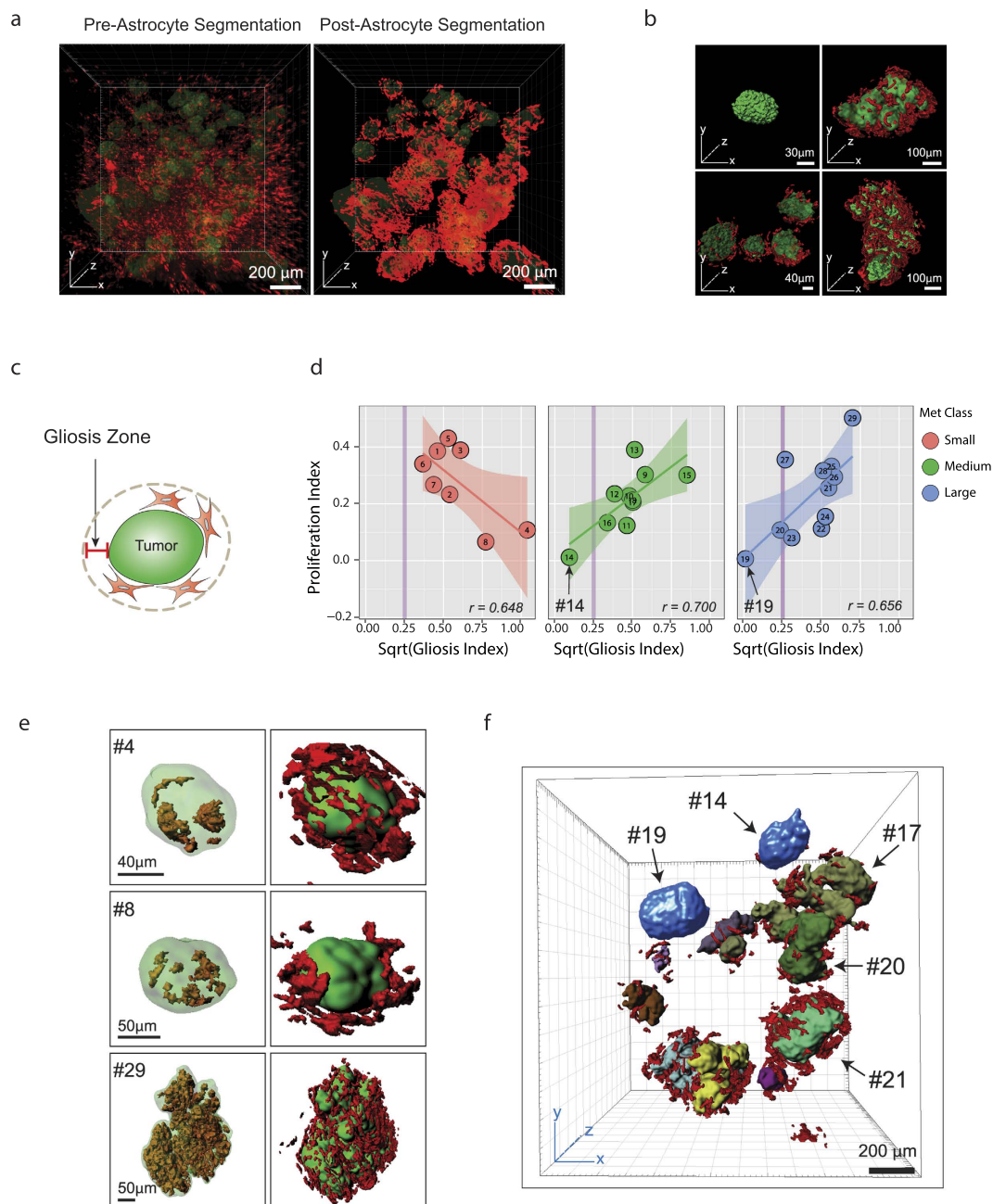


Figure 4. Heterogeneous Astrocyte Response to and Influence on PNA.Met1 Brain Metastases. (a) 3D multiphoton image of astrocytes (GFAP+, red) associated with PNA.Met1 brain metastases (K8, green) (left), and corresponding 3D segmentation of the astrocytes (right). (b) Representative surface generated images of PNA.Met1 tumors (green) and various levels of associated astrocytes (red). (c) Schematic representation of the gliosis zone. Zone depth = 24 μm , the maximum spatial size of one astrocyte. (d) Regression plot of the relationship between the proliferative index and the square root (sqrt) of the gliosis index for small (left), medium (middle), and large (right) PNA.Met1 brain metastases. Gliosis index = Total astrocyte voxel volume/ Total zone voxel volume. (e) Representative surface generated images of PNA.Met1 metastases (green) and EdU-tagged nuclei (orange) (left column) and the metastases and the associated astrocytes (red) (right column). (f) Surface generated image of global view of PNA.Met1 metastases (various colors) and associated astrocytes (red), highlighting tumors extremely low gliosis (blue; #14 and #19).

astrogliosis, was not proliferative, whereas similarly sized tumors (i.e., tumors 17, 20, and 21) within the same metastatic niche as tumor 19 were surrounded with reactive astrocytes and thrived with active proliferation (Fig. 4f), suggesting a role of astrogliosis in sustaining metastasis growth. Unlike PNA.Met1 metastases, global analyses of MDA-MB-231.Br metastases showed no clear correlation between gliosis index, proliferation index, or metastasis size (Supplementary Fig. S4), indicating a non-essential role of astrogliosis in MDA-MB-231.Br

brain metastases. It is likely that the exclusive growth of these metastases along blood vessels (Supplementary Fig. S4a) provides these metastases with a direct nutrient supply that is the ultimate determinant of their outgrowth.

Heterogeneous spatiotemporal angiogenic response to brain metastases. Patterns of brain tumor and brain metastasis angiogenesis are highly debated^{34–36} primarily due to a lack of approaches that can capture blood vessels in their entirety *in situ*. By taking advantage of our tissue clearing-based imaging approach and SMART 3D analysis pipeline, we explored the global intratumoral and peritumoral angiogenesis patterns in 3D (Fig. 5a). Qualitative analyses showed extensive, tortuous tumor-associated vasculature comparable to previous experimental and clinical observations^{37–39}. We also observed highly branched vessels covering the tumor surfaces and few but large infiltrating blood vessels inside the tumors, which were previously underappreciated features (Fig. 5b, Supplementary Fig. S5a, Supplementary Video S4). To reveal the global spatial relationship of each tumor cell to the surrounding blood vessels, we further quantified the spatial distance from each tumor cell voxel to the nearest blood vessel (Fig. 5c). Although metastatic tumors analyzed contain different numbers of tumor cells ($n = 264$ for tumor D and $n = 1136$ for tumor A), as measured by the mode frequency of density curve, most tumor cells were located less than 40 μm away from the nearest blood vessel, a pattern consistent among all metastasis sizes, which is significantly closer than the previously documented limit (100 μm) derived from 2D histology studies⁴⁰.

To further examine the spatial patterns of angiogenesis, we performed concentric zone analysis covering zones from the core of metastases to the closest vessel outside the metastases (Supplementary Fig. 5b,c). Despite different tumor sizes, the maximum relative vascularisation index inside each tumor is approximately 0.02. The vascularisation index of smallest tumor (Tumor D) progressively declined from the tumor surface to the core. Tumor C had an increase of relative vasculature volume approaching the middle zone, after which point the relative vasculature volume sharply decreased, producing an inverted parabola, implying *de novo* angiogenesis inside the tumor.

Finally, to test the whether the SMART 3D-based angiogenesis analysis could potentially be used to evaluate anti-angiogenic therapies, we treated brain metastasis-bearing mice with multi-kinase inhibitor Sorafenib, a FDA approved small molecule inhibitor which has been shown to be blood brain permeable and enter the brain⁴¹ and exhibit encouraging efficacy in treating brain metastases derived from renal cell carcinoma⁴². Surprisingly, despite a discernable decline of peritumoral angiogenesis, the intratumoral mean vascular density (MVD) did not significantly decrease (Fig. 5d).

Discussion

Metastatic colonization and outgrowth are believed to be spatially heterogeneous and temporally dynamic. While current state-of-the-art single-cell sequencing technologies have made strides toward understanding the genetic basis of tumor heterogeneity, deciphering the spatial and compositional heterogeneity of metastasis remains heavily reliant on conventional 2D histology. It is imperative to develop and integrate novel techniques from multiple disciplines to explore metastasis from spatial perspectives. In this study, we sought to do so by further developing and integrating cutting-edge technologies from the fields of both neuroscience and computational science. Our unique, integrative approach combining whole tissue clearing, staining, and imaging, with computer-assisted segmentation and quantifications (SMART 3D) provided us leverage in studying the metastatic landscape with unparalleled accuracy. Specifically, we have demonstrated the power of whole tissue imaging in delineating astonishing morphological diversity of metastatic tumors. More importantly, we demonstrated the feasibility of using multiplexed immunostaining to molecularly characterize the spatially heterogeneous metastasis landscape. With further refinement of whole tissue staining procedures and validation of antibodies for cleared tissue, we expect multiplexed molecular staining will produce unprecedented mechanistic insight into many biological phenomena in the near future.

With the maturation of tissue clearing techniques, using this whole tissue imaging approach to explore tissue structure or tumor heterogeneity becomes highly desirable for many laboratories. However, quantitative analysis of 3D volumetric datasets that are terabytes in size imposes new, significant challenges. Our study provides one possible solution (SMART 3D) for quantitative analysis of 3D, multi-channel volumetric data. First, by developing and applying a spatial background removal algorithm, we effectively removed inhomogeneous fluorescent background present in most biological samples and further induced by immunostaining. Effective background removal in 3D images forms the foundation for downstream segmentation and quantification. Second, we constructed a machine learning (forest classifiers) based multi-channel 3D reconstruction pipeline by integrating biologically meaningful factors annotated by biologists and computational features intrinsic to 3D volumetric datasets. In our experience, applying this machine-learning pipeline is critical to more effectively extract and recover structural information from large 3D volumetric data that inevitably varies significantly within the same dataset. Lastly, our study demonstrated how our integrative whole tissue imaging and analysis platform could help biologists generate statistically significant correlations and discern previously unknown patterns that imply novel hypotheses of molecular mechanisms to be formulated and further explored.

Our study applying our integrative pipeline revealed a previously underappreciated heterogeneity in the metastatic landscape, and our spatial analysis of the metastasis landscape also shed light on how the TME impacts metastatic outgrowth. Two examples of such microenvironmental factors/processes we investigated in our study are astrocytes (in the process of astrogliosis) and vasculature. Through cross-referencing metastasis proliferation, tumor developmental stage, and astrogliosis, we revealed a dual, stage-dependent role of astrocytes on metastatic outgrowth (Fig. 4). Through global proliferation analysis coupled with spatially defined blood vessel density, we noted that the majority of cells in metastatic tumors are located in close proximity (between 10–20 μm) to blood vessels (Fig. 5c). More interestingly, the anti-angiogenic treatments led to a divergent spatial pattern of blood vessel distribution, which should be closely examined in the future studies. Collectively, results from our unbiased

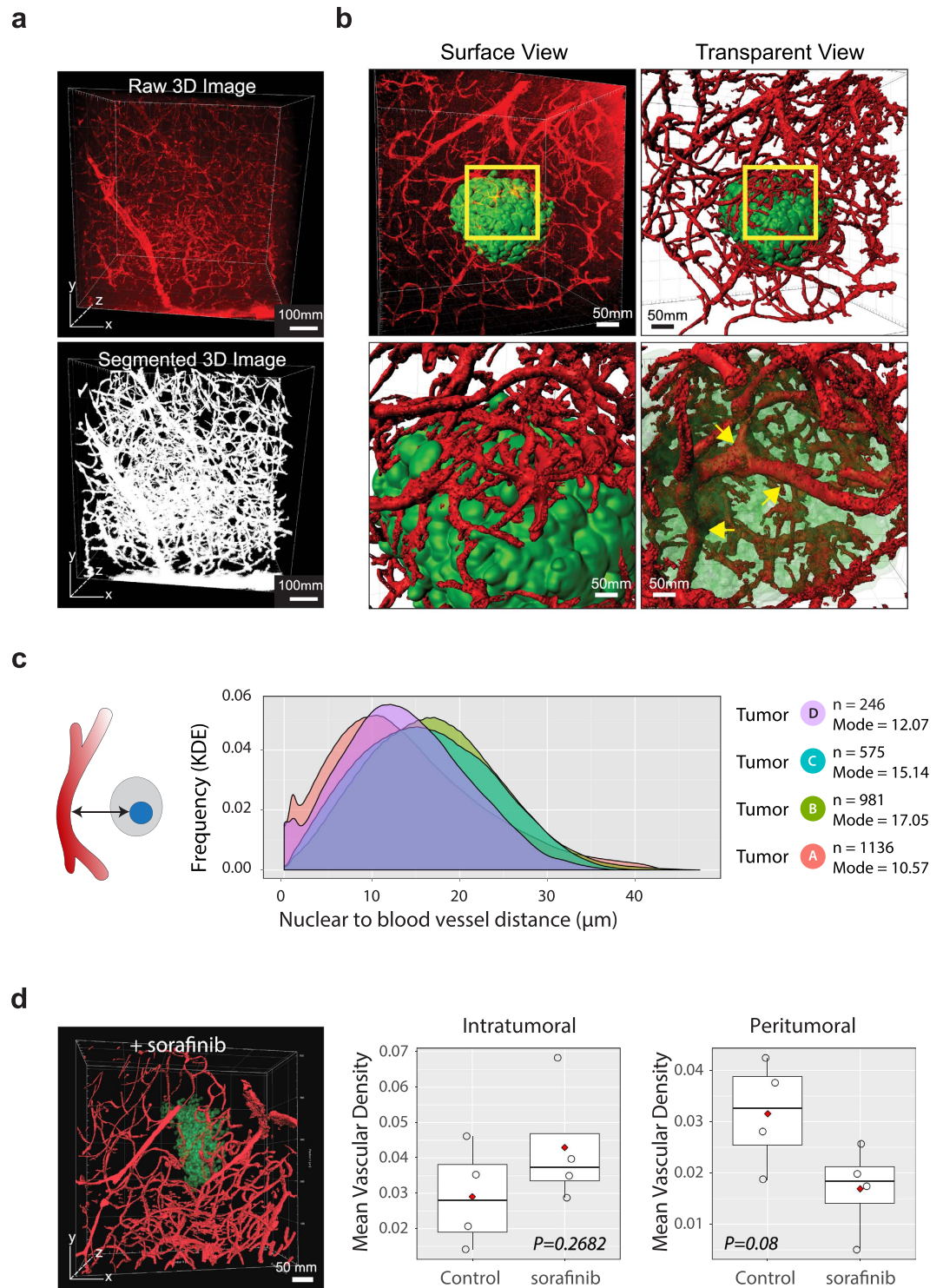


Figure 5. Heterogeneous Spatial and Temporal Vasculature Response to PNA.Met1 Metastases. (a) 3D multiphoton image of metastasis-associated vasculature (top) and associated 3D segmentation image (bottom). (b) 3D images of metastasis-associated vasculature (red) before (top left) and after (top right) surface generation of vasculature, with a focus on vasculature on metastasis surface (bottom left) and infiltrating vasculature (bottom right). (c) Kernel density estimation (KDE) plot for the distance of each tumor cell voxel to the nearest blood vessel for tumors A, B, C, and D. *n*: number of tumor cells. (e) Surface generated image of a PNA.Met1 brain metastasis (transparent green) and associated vasculature (red) treated with Sorafenib (left) and plots of the mean vasculature density within the tumor (intratumoral) and outside the tumor (peritumoral) for Sorafenib and control-treated mice. Peritumoral zone = spatial distance within 100 μm from tumor surface.

global approach further underscore a critical role of metastatic niche environmental factors and their potential role in sustaining metastatic outgrowth or metastatic dormancy. These observations will lead to new avenues for further functional investigations of novel mechanisms of metastasis.

With the continuous development of new, better tissue clearing methods and optics technology, our platform and SMART 3D will only grow in relevance. Our platform is designed to be able to integrate any given tissue clearing method, and SMART 3D is capable of processing and analyzing image data sets derived from a variety of 3D, multi-channel high content imaging strategies. In this study, we demonstrated the ability of SMART 3D to adapt to analyzing datasets derived from the most recently developed tissue clearing methods, including CUBIC 2, PACT, and ScaleAB^{43–45}. Furthermore, our platform will become even more vital for researchers applying new tissue clearing methods, which are increasingly compatible with multiple antibodies (Supplementary Table S2). Increasing ability to simultaneously stain for multiple markers will dictate the use of several channels during image acquisition, necessitating the multi-channel processing and analysis of which our platform is uniquely capable. Advanced optics systems for imaging will decrease image acquisition time while increasing the data content obtained, which SMART 3D will be able to process and analyze. Our integrative pipeline, unlike most methods and technologies, promises to become increasingly relevant with time and provide a scaffold by which researchers can tackle complex biological questions.

Taken together, we developed an integrative platform for 3D quantitative analysis of the spatially and compositionally heterogeneous metastasis landscape. Using whole tissue multiplexed staining and fluorescence imaging coupled with our SMART 3D image analysis pipeline, we demonstrated intriguing patterns of spatial heterogeneity of the metastatic landscape. By integrating multidisciplinary expertise, our proof-of-concept study, the first of this type, further demonstrates the necessity of examining metastases in 3D *in situ*, the practicality of this approach, and the novel concepts and discoveries that may be derived from 3D quantitative image analysis.

Methods

Cell Culture. The parental MDA-MB-231 cells were purchased from ATCC. MDA-MB-231.Br cell line was developed by *in vivo* selection of brain tropic derivatives for a minimum of three rounds through intra-cardiac injection. PNA.Met1 cell lines were established from spontaneous primary murine mammary tumors from MMTV-PyMT transgenic mouse (FVB background). MDA-MB-231.Br cell line was cultured in DMEM F12 medium supplemented with 10% fetal bovine serum (FBS) and 1% penicillin streptomycin (Pen-Strep). PNA.Met1 cells were cultured in DMEM high glucose medium supplemented with 10% FBS and 1% Pen-Strep. Both cell lines were maintained at 37 °C in a 5% CO₂ humidified environment and subcultured upon reaching approximately 85% confluence. Immediately prior to injection, cells were rinsed three times with 1 × PBS, trypsinized, and pelleted twice and resuspended in serum-free RPMI medium to a concentration of approximately two million cells/mL.

Brain Metastasis Mouse Models and *In Vivo* Experiments. All animal experiments were performed ethically and in accordance with IACUC protocol approved by the University of Notre Dame IACUC committee. FVB and congenic Rag1^{-/-} (C.129S7(B6)-Rag1^{tm1Mom/J}) mice were purchased from The Jackson Laboratory (Bar Harbor, ME). All mice were eight weeks or older prior to experimental procedures. *In vivo* brain metastases were formed by either injection of 100 μL (~200,000 cells) cell suspension via the right internal carotid artery or intra-cranial injection of 690 nL of ~70,000 cells (drug treatment experiments). Prior to and during injection of cancer cells, mice were anesthetized with isoflurane. Following surgery, mice received 100 μL subcutaneous injections of Baytril[®] (2.27%, Bayer HealthCare LLC, Animal Health Division), Ketoprofen[®] (1 mg/mL) and 1 mL of 0.9% NaCl. FVB mice injected with PNA.Met1 cells were sacrificed after two weeks following cell injection, while the Rag1^{-/-} mice injected with MDA-MB-231Br cells were sacrificed between three to four weeks after injection. Two hours prior to sacrifice, mice were injected with 100 μL of 100 mg/mL 5-ethynyl-2'-deoxyuridine (EdU, Life Technologies, Cat. No. 10639) via tail vein. For labeling blood vasculature, animals were injected with 100 μL 10,000 MW Dextran, Alexa Fluor[®] 488 or Alexa Fluor[®] 594 (Life Technologies[™], Cat. No. D-22910 or D-22913) via tail vein five minutes prior to sacrifice when the brain was intended to be put through PACT or CUBIC tissue clearing. In instances when the brain was intended to be cleared by the ScaleAB protocol, cardiac perfusion with 10 mL or DiR (Sigma, Cat. No. 43608) was performed as described previously⁴⁶. Immediately prior to and during sacrificing, mice were anesthetized with isoflurane. Mice that did not receive a Dextran injection or were not perfused with DiR were perfused transcatheterially with 10 mL chilled 1 × PBS immediately followed by 10 mL chilled 4% paraformaldehyde (PFA). Mice that did receive a Dextran injection were not perfused. Brains were extracted, cut in half sagittally, and placed in 4% PFA for 24 hours at 4 °C with gentle rocking. For anti-angiogenic treatment experiments, Sorafenib (LC Laboratories, Woburn, MA) was administered to mice at a concentration of 50 mg/kg by intra-peritoneal injection once daily 10 days following metastasis induction. Sorafenib was diluted in Cremophore EL (Sigma

Tissue Clearing and Staining. Slightly modified CUBIC and PACT tissue clearing protocols^{43,47} were used as follows for brain tissue clearing, with the exception of the Sorafenib treated brains. Following 24 hours fixation, brains were rinsed twice with 1 × PBS, sliced into 2 mm sagittal sections, and incubated in a hydrogel formulation (2 or 4% acrylamide in 1 × PBS with 0.25% photoinitiator VA044 [Wako Chemicals]) at 4 °C gently rocking for three days. Prior to hydrogel polymerization, samples were degassed using a desiccation chamber, alternating between three 10-minute cycles of vacuum and nitrogen gas. Samples were polymerized by incubation at 37 °C for 3–4 hours. Polymerized hydrogel was decanted and samples were rinsed twice with 1 × PBS. Lipid removal from samples was then performed using either 8% SDS in 1 × PBS. Once samples became optically transparent after approximately 4–7 days, samples were washed for 24 hours in 1 × PBS before whole tissue staining (molecular phenotyping). For molecular phenotyping, all samples were first incubated in a 1:50 primary antibody dilution

(anti-Ms mAb GFAP (GA5), Cell Signaling Technology Technologies[®], Cat. No. 3670s; anti-Rb mAb Cytokeratin 8 (EP1928Y), Abcam[®], Cat. No. ab53280) in 0.1% Triton X-100 for 3 to 7 days with gentle rotating. Following primary antibody incubation, samples were washed for 24 hours in 0.1% Triton X-100 with minimum three rounds of buffer changes. All samples were then incubated in a 1:50 secondary antibody (goat anti-Rb or goat anti-Ms Alexa Fluor[®] 488, 594, or 647) dilution in 0.1% Triton X-100 for 3 to 7 days with gentle rotating. After secondary antibody incubation, EdU was detected per Click-iT EdU Alexa Fluor[®] 488 or 594 imaging kit (Life Technologies[™], Cat. No. 10639) protocol with a 3–4 hour detection incubation period. Some samples were incubated in DAPI (0.025 mg/mL) for 12 hours with gentle rotating. Samples were washed one last time in 0.1% Triton X-100 for 24 hours with multiple buffer changes and then made optically transparent by incubation in CUBIC 2 reagent prepared as described previously⁴³ for at least 2 hours prior to imaging. The brains of Sorafinib treated mice were cleared using ScaleAB methodology as previously described⁴⁴.

Confocal and Two-Photon Microscopy. All images were acquired using either the confocal or two-photon setting on a commercial multiphoton laser scanning inverted microscope (Olympus FV1000) equipped with filter set (460–500, 520–560, 525–625, 650–700 nm) and a mode-locked Ti:sapphire laser (Mai Tai DeepSee 690–1040 nm, Spectra-Physics). Optical cleared and stained samples were immersed in CUBIC 2 reagent in a custom-made sample holder when imaged using a 10× ScaleView objective (XLPLN10XSVM, Olympus USA; NA = 0.6 and WD = 8 mm) or placed on a coverslip when imaged using the 25× objective (XLSLPLN25XGMP, Olympus USA; NA = 1.0 and WD = 8 mm). Use of confocal versus multiphoton was dictated by which method better excited the Alexa fluorophores, which depended on fluorophore vendor and imaging depth. When acquiring images to be stitched, MATL was used in the Olympus software to program 10% overlap between imaging stacks.

Image Processing and Segmentation. *Background removal.* Auto-fluorescence in mouse brains results in a strong and inhomogeneous background in the acquired 3D images. Such inhomogeneous background (noise) causes difficulties to segmentation and visualization of the 3D images. We developed a new approach¹⁹ that combines the spatial filtering method and optimization-based methods for this background removal problem. First, we applied percentile filtering with a window size that is slightly bigger than the size of the smallest object (e.g., the size of a cell) in the image, to estimate a rough background. Then, we used unsupervised one-class learning²¹ to detect errors in this rough estimation. Finally, these errors were corrected in the re-estimation process and the refined background estimation was obtained for generating a noise-free image. The processing speed of our new background removal method¹⁹ is comparable to the rolling ball algorithm²⁰ and yields the state-of-the-art accuracy. More details and validations can be found in¹⁹.

Voxel-level segmentation. We utilized information from multiple channels (e.g. K8, DAPI, GFAP, and EdU) for segmentation. For this purpose, we formulated the voxel-level segmentation problem as a classification problem. Several classifiers were trained to determine whether a voxel belongs to a specific type of foreground (tumor cells, astrocytes, blood vessels, etc) or the background based on multi-channel features. These classifiers were then applied to every voxel in the 3D image to generate the segmentation.

(1) *Multi-channel feature extraction:* The classification accuracy relies heavily on the quality of the extracted features. In order to utilize multi-channel information, our multi-channel feature extraction procedure for the voxels consists of two main steps. (i) Extracting a feature vector in each channel. As in⁴⁸, the following features are extracted for every voxel in each channel to represent its appearance and texture: Intensity, gradient magnitude, eigenvalues of the Hessian matrix, and eigenvalues of structure tensor; (ii) concatenating together feature vectors from different channels to form a multi-channel feature vector. (2) *Voxel classification:* After the feature extraction process, training data were labeled by human experts and used to train four random forest classifiers⁴⁹ that were designed to classify tumor cells, astrocytes, proliferating cells, and blood vessels. Each classifier has 200 trees and 2 candidate features in each node. These classifiers are then applied to every voxel in the 3D image to generate segmentation results.

Structural-level segmentation. Since tumor cells tend to form dense clusters, to eliminate false-positives, cell clusters whose volumes are larger than a threshold in the voxel-level segmentation of tumor cells were identified as tumor clusters. The volume of each cell cluster was approximated by the volume of its connected component in the voxel-level segmentation. The threshold for large clusters was selected by a human expert for each 3D image. When K8 staining was used, each cell cluster that contains K8 signal was immediately identified as a tumor cluster regardless of its size.

Image Quantification. Based on the structural-level segmentation and voxel-level segmentation, we performed the following quantifications. (1) *Proliferation ratio:* By assuming that every cell of a specific type has an average volume, the proliferation ratio of each tumor cluster can be determined approximately as the ratio of the volume of proliferating cells inside the tumor to the volume of the tumor cluster. The volume of proliferating cells was computed based on their voxel-level segmentation and the volume of the tumor cluster was computed as describe above. (2) *Volume of surrounding astrocytes (astrogliosis):* For each tumor cluster, we define its surrounding space as consisting of all the voxels that satisfy the following two conditions: (a) It is outside the tumor cluster, and (b) its closest distance to the tumor surface is smaller than a chosen value *dis* (the average diameter of an astrocyte is 24 μm. Therefore we set *dis* = 24 μm to survey the single layer of astrocytes surrounding the tumor for astrocytes). The surrounding space was calculated in two steps: (i) dilate the cluster region in the original image in a spherical manner with a radius *dis*; (ii) subtract the original cluster region from the dilated region. Then the volume of the surrounding astrocytes can be easily calculated. (3) *Zone analysis:* Zone analysis was performed in

a similar manner. Each zone was calculated using image morphological or logical operations. (4) *Distribution of the closest distances from tumor cells to blood vessels*: We computed approximately the distribution of the closest distances from tumor cells to blood vessels by computing the distribution of the closest distances from tumor cell voxels to blood vessel voxels, which was carried out by using the k-nearest neighbor search function in MATLAB.

3D Volumetric Data Presentation. 3D images were obtained by stacking up and aligning 2D image slices based on minimizing the mean squared error (MSE) between aligned regions in consecutive slices using a custom MATLAB code and XUVStitch (<http://www.xuvtools.org>). All surface generated images and videos of original data or surface generated data were created using IMARIS software (Bitplane).

Raw quantification data were extracted by using MATLAB, and statistical analysis was performed in R studio. $P < 0.05$ (two-tailed) was considered statistically significant.

References

- Hanahan, D. & Weinberg, R. A. Hallmarks of Cancer: The Next Generation. *Cell* **144**, 646–674 (2011).
- Quail, D. F. & Joyce, J. A. Microenvironmental regulation of tumor progression and metastasis. *Nat. Med.* **19**, 1423–1437 (2013).
- Zellmer, V. R. & Zhang, S. Evolving concepts of tumor heterogeneity. *Cell Biosci.* **4**, 69 (2014).
- Kodack, D. P., Askoxylakis, V., Ferraro, G. B., Fukumura, D. & Jain, R. K. Emerging Strategies for Treating Brain Metastases from Breast Cancer. *Cancer Cell* **27**, 163–175 (2015).
- Karnoub, A. E. *et al.* Mesenchymal stem cells within tumour stroma promote breast cancer metastasis. *Nature* **449**, 557–563 (2007).
- Psaila, B. & Lyden, D. The metastatic niche: adapting the foreign soil. *Nat. Rev. Cancer* **9**, 285–293 (2009).
- Fidler, I. J., Yano, S., Zhang, R.-D., Fujimaki, T. & Bucana, C. D. The seed and soil hypothesis: vascularisation and brain metastases. *Lancet Oncol.* **3**, 53–57 (2002).
- Zheng, H. & Kang, Y. Cradle of Evil: Osteogenic Niche for Early Bone Metastasis. *Cancer Cell* **27**, 153–155 (2015).
- O'Brien, E. R. *et al.* Glial activation in the early stages of brain metastasis: TSPO as a diagnostic biomarker. *J. Nucl. Med. Off. Publ. Soc. Nucl. Med.* **55**, 275–280 (2014).
- Fidler, I. J., Yano, S., Zhang, R.-D., Fujimaki, T. & Bucana, C. D. The seed and soil hypothesis: vascularisation and brain metastases. *Lancet Oncol.* **3**, 53–57 (2002).
- Tate, M. C. & Aghi, M. K. Biology of angiogenesis and invasion in glioma. *Neurother. J. Am. Soc. Exp. Neurother.* **6**, 447–457 (2009).
- Guldner, I. H. & Zhang, S. A journey to uncharted territory: new technical frontiers in studying tumor–stromal cell interactions. *Integr. Biol.* **7**, 153–161 (2015).
- Richardson, D. S. & Lichtman, J. W. Clarifying Tissue Clearing. *Cell* **162**, 246–257 (2015).
- Valiente, M. *et al.* Serpins Promote Cancer Cell Survival and Vascular Co-Option in Brain Metastasis. *Cell* **156**, 1002–1016 (2014).
- Seike, T. *et al.* Interaction between lung cancer cells and astrocytes via specific inflammatory cytokines in the microenvironment of brain metastasis. *Clin. Exp. Metastasis* **28**, 13–25 (2011).
- Kim, S.-J. *et al.* Astrocytes Upregulate Survival Genes in Tumor Cells and Induce Protection from Chemotherapy. *Neoplasia N. Y. N* **13**, 286–298 (2011).
- Susaki, E. A. *et al.* Whole-Brain Imaging with Single-Cell Resolution Using Chemical Cocktails and Computational Analysis. *Cell* **157**, 726–739 (2014).
- Yang, B. *et al.* Single-cell phenotyping within transparent intact tissue through whole-body clearing. *Cell* **158**, 945–958 (2014).
- Yang, L., Zhang, Y., Guldner, I. H., Zhang, S. & Chen, D. Z. in *Medical Image Computing and Computer-Assisted Intervention — MICCAI 2015* (eds Navab, N., Hornegger, J., Wells, W. M. & Frangi, A. F.) 292–299 (Springer International Publishing, 2015).
- Collins, T. J. ImageJ for microscopy. *BioTechniques* **43**, 25–30 (2007).
- Liu, W., Hua, G. & Smith, J. R. Unsupervised One-Class Learning for Automatic Outlier Removal. In *2014 IEEE Conference on Computer Vision and Pattern Recognition (CVPR)* 3826–3833 (2014). Date of access: 10/15/2015.
- Powers, D. M. Evaluation: from Precision, Recall and F-measure to ROC, Informedness, Markedness and Correlation. *J. Mach. Learn. Tech.* **2**, 37–63 (2011).
- Carbonell, W. S., Ansoorge, O., Sibson, N. & Muschel, R. The Vascular Basement Membrane as ‘Soil’ in Brain Metastasis. *PLoS One* **4**, 10.1371/journal.pone.0005857 (2009).
- Salic, A. & Mitchison, T. J. A chemical method for fast and sensitive detection of DNA synthesis *in vivo*. *Proc. Natl. Acad. Sci. USA* **105**, 2415–2420 (2008).
- Fidler, I. J. The pathogenesis of cancer metastasis: the ‘seed and soil’ hypothesis revisited. *Nat. Rev. Cancer* **3**, 453–458 (2003).
- O'Brien, E. R., Howarth, C. & Sibson, N. R. The role of astrocytes in CNS tumors: pre-clinical models and novel imaging approaches. *Front. Cell. Neurosci.* **7**, 40 (2013).
- O'Brien, E. R. *et al.* Glial activation in the early stages of brain metastasis: TSPO as a diagnostic biomarker. *J. Nucl. Med. Off. Publ. Soc. Nucl. Med.* **55**, 275–280 (2014).
- De Oliveira Barros, E. G. *et al.* The reciprocal interactions between astrocytes and prostate cancer cells represent an early event associated with brain metastasis. *Clin. Exp. Metastasis*, doi: 10.1007/s10585-014-9640-y (2014).
- Fitzgerald, D. P. *et al.* Reactive glia are recruited by highly proliferative brain metastases of breast cancer and promote tumor cell colonization. *Clin. Exp. Metastasis* **25**, 799–810 (2008).
- Seike, T. *et al.* Interaction between lung cancer cells and astrocytes via specific inflammatory cytokines in the microenvironment of brain metastasis. *Clin. Exp. Metastasis* **28**, 13–25 (2011).
- Xing, F. *et al.* Reactive astrocytes promote the metastatic growth of breast cancer stem-like cells by activating Notch signalling in brain. *EMBO Mol. Med.* **5**, 384–396 (2013).
- Wang, L. *et al.* Astrocytes Directly Influence Tumor Cell Invasion and Metastasis *in Vivo*. *PLoS One* **8**, e80933 (2013).
- Kim, S.-J. *et al.* Astrocytes Upregulate Survival Genes in Tumor Cells and Induce Protection from Chemotherapy. *Neoplasia N. Y. N* **13**, 286–298 (2011).
- Langley, R. R. & Fidler, I. J. The biology of brain metastasis. *Clin. Chem.* **59**, 180–189 (2013).
- Fidler, I. J., Yano, S., Zhang, R.-D., Fujimaki, T. & Bucana, C. D. The seed and soil hypothesis: vascularisation and brain metastases. *Lancet Oncol.* **3**, 53–57 (2002).
- Bugyik, E. *et al.* Lack of angiogenesis in experimental brain metastases. *J. Neuropathol. Exp. Neurol.* **70**, 979–991 (2011).
- Jain, R. K. *et al.* Angiogenesis in brain tumours. *Nat. Rev. Neurosci.* **8**, 610–622 (2007).
- Huang, Y., Goel, S., Duda, D. G., Fukumura, D. & Jain, R. K. Vascular Normalization as an Emerging Strategy to Enhance Cancer Immunotherapy. *Cancer Res.* **73**, 2943–2948 (2013).
- Kienast, Y. *et al.* Real-time imaging reveals the single steps of brain metastasis formation. *Nat. Med.* **16**, 116–122 (2010).
- Fidler, I. J., Yano, S., Zhang, R., Fujimaki, T. & Bucana, C. D. The seed and soil hypothesis: vascularisation and brain metastases. *Lancet Oncol.* **3**, 53–57 (2002).
- Steege, P. S., Camphausen, K. A. & Smith, Q. R. Brain metastases as preventive and therapeutic targets. *Nat. Rev. Cancer* **11**, 352–363 (2011).

42. Massard, C. *et al.* Incidence of brain metastases in renal cell carcinoma treated with sorafenib. *Ann. Oncol.* mdp411, doi:10.1093/annonc/mdp411 (2010).
43. Susaki, E. A. *et al.* Whole-Brain Imaging with Single-Cell Resolution Using Chemical Cocktails and Computational Analysis. *Cell* **157**, 726–739 (2014).
44. Hama, H. *et al.* ScaleS: an optical clearing palette for biological imaging. *Nat. Neurosci.* **18**, 1518–1529 (2015).
45. Yang, B. *et al.* Single-cell phenotyping within transparent intact tissue through whole-body clearing. *Cell* **158**, 945–958 (2014).
46. Li, Y. *et al.* Direct labeling and visualization of blood vessels with lipophilic carbocyanine dye DiI. *Nat. Protoc.* **3**, 1703–1708 (2008).
47. Yang, B. *et al.* Single-cell phenotyping within transparent intact tissue through whole-body clearing. *Cell* **158**, 945–958 (2014).
48. Sommer, C., Straehle, C., Kothe, U. & Hamprecht, F. A. Ilastik: Interactive learning and segmentation toolkit. in *2011 IEEE International Symposium on Biomedical Imaging: From Nano to Macro* 230–233, doi:10.1109/ISBI.2011.5872394 (2011).
49. Liaw, A. & Wiener, M. Classification and Regression by randomForest. *R News* **2**, 18–22 (2002).

Acknowledgements

We would like to thank Dr. Charles Tessier at Indiana University School of Medicine South Bend and Richard Heil-Chapdelaine at Olympus USA for invaluable technical support. We would like to thank Dr. Calli A. Versagli for technical support and Zhang Lab members for insightful discussions of this project. This work was partially supported by NIH Pathway to Independence Award 5R00CA158066-05 (SZ), NIH 1R01CA194697-01 (SZ), Walther Cancer Foundation Advancing Basic Cancer Research Grant II (SZ), Department of Defense W81XWH-15-1-0021 (SZ), Indiana CTSI core pilot fund (SZ), and NSF Grant CCF-1217906 (DZC). Dr. S. Zhang is the Nancy Dee Assistant Professor in Cancer Research at University of Notre Dame.

Author Contributions

I.H.G., L.Y. and S.Z. developed the original hypothesis and designed experiments. I.H.G., K.R.C., Q.W., W.V.A., V.R.Z., M.H. and S.Z. performed experiments. I.H.G., L.Y., K.R.C., Y.Z., F.L., D.Z.C. and S.Z. analyzed data. I.H.G., L.Y., V.R.Z. and S.Z. wrote and edited the manuscript. S.Z. supervised the study.

Additional Information

Supplementary information accompanies this paper at <http://www.nature.com/srep>

Competing financial interests: The authors declare no competing financial interests.

How to cite this article: Guldner, I. H. *et al.* An Integrative Platform for Three-dimensional Quantitative Analysis of Spatially Heterogeneous Metastasis Landscapes. *Sci. Rep.* **6**, 24201; doi: 10.1038/srep24201 (2016).



This work is licensed under a Creative Commons Attribution 4.0 International License. The images or other third party material in this article are included in the article's Creative Commons license, unless indicated otherwise in the credit line; if the material is not included under the Creative Commons license, users will need to obtain permission from the license holder to reproduce the material. To view a copy of this license, visit <http://creativecommons.org/licenses/by/4.0/>

GAD1 Upregulation Programs Aggressive Features of Cancer Cell Metabolism in the Brain Metastatic Microenvironment



Patricia M. Schnepf^{1,2}, Dennis D. Lee¹, Ian H. Guldner^{1,2}, Treasa K. O'Tighearnaigh¹, Erin N. Howe^{1,2}, Bhavana Palakurthi¹, Kaitlyn E. Eckert³, Tiffany A. Toni³, Brandon L. Ashfeld^{2,3}, and Siyuan Zhang^{1,2,4}

Abstract

The impact of altered amino acid metabolism on cancer progression is not fully understood. We hypothesized that a metabolic transcriptome shift during metastatic evolution is crucial for brain metastasis. Here, we report a powerful impact in this setting caused by epigenetic upregulation of glutamate decarboxylase 1 (GAD1), a regulator of the GABA neurotransmitter metabolic pathway. In cell-based culture and brain metastasis models, we found that downregulation of the DNA methyltransferase DNMT1 induced by the brain microenvironment-derived clusterin resulted in decreased GAD1 promoter methylation and subsequent upregulation of GAD1 expression in brain metastatic tumor cells. In a system to dynamically visualize cellular meta-

bolic responses mediated by GAD1, we monitored the cytosolic NADH:NAD⁺ equilibrium in tumor cells. Reducing GAD1 in metastatic cells by primary glia cell coculture abolished the capacity of metastatic cells to utilize extracellular glutamine, leading to cytosolic accumulation of NADH and increased oxidative status. Similarly, genetic or pharmacologic disruption of the GABA metabolic pathway decreased the incidence of brain metastasis *in vivo*. Taken together, our results show how epigenetic changes in GAD1 expression alter local glutamate metabolism in the brain metastatic microenvironment, contributing to a metabolic adaptation that facilitates metastasis outgrowth in that setting. *Cancer Res*; 77(11); 2844–56. ©2017 AACR.

Introduction

Altered cancer cell metabolism has been recognized as one of the important hallmarks of cancer (1, 2). The dynamic metabolic balance between metabolic stress and the high demand for macromolecules for enhanced proliferation in the tumor cell is highly tissue context dependent (1). The process of metastasis represents an extreme case of context-dependent metabolic adaptation (3). Recently, experimental evidence began to shed light on the critical role of the metabolic interactions between tumor cells and the metastatic tumor microenvironment in facilitating metastatic success. Direct lipid transfer from peritoneal adipocytes to metastatic ovarian cancer cells promotes omental metastasis (4). Colon cancer cell-derived creatine kinase promotes the synthesis of phosphocreatine, which is transported and catabolized by meta-

static tumor cells to generate ATP (5). In addition, an *in vitro* proteomics analysis of brain-seeking subclones of a breast cancer cell line showed an increase in proteins that regulates β -oxidation of fatty acid synthesis, glycolysis, and citric acid cycle (TCA) cycle activity compared with the parental lines, implying a role for the brain microenvironment in reshaping metastatic tumor cell metabolism (6). Yet, the mechanisms of how metastatic tumor cells acquire a new metabolic balance when surrounded by a highly metabolically unique brain microenvironment are still poorly understood.

In normal physiologic conditions, the brain microenvironment displays a unique metabolic cooperation among diverse cells types. Global brain tissue metabolism is compartmentalized between different cellular subtypes (7). This compartmentalized metabolic phenotype requires dynamic cross-talk between various cell types to establish a cohesive metabolic signaling network (8, 9). Highly active neurons require an uninterrupted supply of metabolites from the astrocyte–neuron metabolic shuttle: lactate, glutamate, glutamine, malate, and α -ketoglutarate (10–13). Interestingly, recent studies have revealed cross-talk between brain astrocytes and metastatic tumor cells that is reminiscent of astrocyte–neuron interactions, including downregulation of the tumor suppressor PTEN through the uptake of glia-derived exosomes (14), and gap junction-mediated transfer of cGAMP to astrocytes (15). Intriguingly, clinical brain metastases display an increased neuronal-like gene signature compared with primary tumor counterparts, suggesting metastatic tumor cells engage an extensive brain-like transcriptome adaptation (16, 17). However, it is still unknown whether the neuronal-like properties obtained by

¹Department of Biological Sciences, College of Science, University of Notre Dame, Notre Dame, Indiana. ²Mike and Josie Harper Cancer Research Institute, University of Notre Dame, South Bend, Indiana. ³Department of Chemistry and Biochemistry, University of Notre Dame, Notre Dame, Indiana. ⁴Indiana University Melvin & Bren Simon Cancer Center, Indianapolis, Indiana.

Note: Supplementary data for this article are available at Cancer Research Online (<http://cancerres.aacrjournals.org/>).

Corresponding Author: Siyuan Zhang, Department of Biological Sciences, University of Notre Dame, A130 Harper Hall, Notre Dame, IN 46556. Phone: 574-631-4635; Fax: 574-631-2156; E-mail: szhang8@nd.edu

doi: 10.1158/0008-5472.CAN-16-2289

©2017 American Association for Cancer Research.

the metastatic tumor cell facilitate a neuronal-like metabolic adaption to efficiently utilize the metabolites in the extracellular compartment of the brain.

In this study, we identified the brain microenvironment-dependent upregulation of glutamate decarboxylase 1 (GAD1) in metastatic cancer cells, which facilitates glutamine metabolism and intracellular γ -aminobutyric acid (GABA) production. Mechanistically, we elucidated that epigenetic regulation induced by the brain microenvironment-derived clusterin resulted in an upregulation of GAD1 expression and functionally necessitated sustained brain metastatic outgrowth. Furthermore, our results revealed a novel therapeutic opportunity for brain metastasis patients. GAD1-GABA-dependent metastasis outgrowth warrants an alternative therapeutic strategy by repurposing FDA-approved blood-brain barrier (BBB)-permeable GABA-targeting agent. Here, we demonstrate that vigabatrin, a clinically approved antiepileptic seizure drug targeting the catabolism of GABA downstream of GAD1, showed a promising therapeutic efficacy in treating brain metastasis *in vivo*. In summary, our study provides mechanistic insight into brain microenvironment-induced epigenetic regulation of GAD1. Our preclinical evidence of repurposing antiseizure agents as novel anti-brain metastatic treatment opens new translational avenues, which could yield more effective clinical therapeutics for patients who are desperate for a cure.

Materials and Methods

Reagents and cell culture

A375SM and MDA-MB-231 cell lines were purchased from ATCC in the past 3 years and cultured less than 6 months before replenishment. Cells were authenticated by short tandem repeat less than 6 months prior to publication. All cell lines were tested mycoplasma negative. Human cell lines were further authenticated using STR profiling by Genetica DNA Laboratories. Primary glia cells were isolated from the brain tissue of newborn C57B6 mouse pups (1–3 days old) as described previously (18). Cancer-associated fibroblast (CAF) cell line was a gift from Dr. Zachary Schafer at the University of Notre Dame (Notre Dame, IN). Lentiviral-based expression vectors pcDNA3/Myc-DNMT1 (36939), pcDNA3.1-Peredox-mCherry (32383), and packaging vectors were purchased from Addgene. Lentiviral-based TRIPZ short hairpin RNA (shRNA) and SMARTpool:ON-TARGETplus siRNA were purchased from GE Healthcare. MISSION esiRNA and GABRA1 (HPA055746) antibodies were purchased from Sigma-Aldrich. DNMT3A (ab4897) and p-AMPK (ab131357) antibodies were purchased from Abcam. DNMT1 (5032) and DNMT3B (67259) antibodies were purchased from Cell Signaling Technology. For coculture experiments, tumor cells were mixed in a 1:5 ratio with either freshly isolated primary glia or CAF cells in 6-well plates. For the transwell coculture experiments, tumor cells were seeded in the bottom wells, and primary glia or CAF cells were seeded on the upper insert and maintained for 2 days. For conditioned media and coculture experiments, reduced media (1 g/L glucose, 2 mmol/L L-glutamine, 10% of FBS, and 1% penicillin/streptomycin) were used. Conditioned media were collected 5 days after seeding of either glia or CAF cells. Conditioned media were mixed with fresh media as designated and used as culture media for tumor cell proliferation assay. Cytokine array analysis was conducted by RayBiotech (Quant-

body Mouse Cytokine Array 4000). Human clusterin protein (2937-HS-050) was purchased from R&D Systems. Clusterin siRNA (mouse, sc-43689) was purchased from Santa Cruz Biotechnology.

Bioinformatics and gene set enrichment analysis

Publicly available GSE19184 dataset (17) was analyzed for transcriptome changes of tumor cell at the different tissue microenvironments. In brief, we performed differential gene expression analysis using the Comparative Selection Marker Module interface to compare the transcriptome profile of brain metastases to respective primary tumor. Four tumor types were analyzed: MDA-MB-231Br3 for mammary tumor, PC14Br4 for prostate tumor, A375SM for melanoma, and KM12M for cecum cancer. A q-value of less than 0.05 was considered statistically significant. To identify metabolism-related genes, we performed gene set enrichment analysis (GSEA; ref. 19) using GenePattern interface (<http://www.broadinstitute.org/gsea/>; ref. 20). Metabolism-specific custom gene sets were assembled from the MSigDB v4.0 database (19), specifically from c2 and c5 subdatabases. GSEA enrichment results were compared across all four cell lines to identify shared enriched gene sets. The differently expressed metabolic genes were depicted by Java Treeview. Network analysis was conducted through the web-based bioinformatics package NetworkAnalyst (<http://www.networkanalyst.ca>) based on recommended protocol (21, 22).

qRT-PCR

Total RNA was isolated using TRIzol reagent (Life Technologies) and then reverse transcribed using Verso cDNA Synthesis Kit (Thermo Fisher Scientific). SYBR-based qRT-PCR was performed using predesigned primers. For quantification of gene expression, real-time PCR was conducted using iTaq Universal SYBR Green Supermix (Bio-Rad) on a Mastercycler ep *realplex* real-time PCR machine (Eppendorf). The relative expression of mRNAs was quantified by $2^{-\Delta\Delta C_t}$ with logarithm transformation.

Proliferation assay

Tumor cells were seeded in 1:5 ratio of tumor to stromal cell and cultured for 48 hours in reduced media. Five random nonoverlapping regions were imaged using a Zeiss Axio confocal microscope. Three wells were manually counted for each condition.

DNA extraction and methylation analysis

Genomic DNA was extracted from 25 mg of brain tissue containing human metastatic tumors or 100,000 tumor cells with the DNeasy Blood and Tissue Kit (Qiagen). DNA (1 μ g) was modified with sodium bisulfite (EpiTect Kit, Qiagen). For methylation-specific PCR, 100 ng of converted DNA was amplified with the EpiTect MSP Kit (Qiagen) using specific methylated or unmethylated primers designed with MethPrimer (23) and following the cycling conditions indicated by the EpiTect MSP Kit. For bisulfite sequencing, GAD1 promoter region (CpG island 122) was amplified and gel was purified. Sanger DNA sequencing was performed on purified PCR amplicon.

Biosensors and time-lapse imaging

Tumor cells were transiently transfected with Peredox (24) and cocultured with either CAF or glia cells in reduced media conditions for 48 hours. For time-lapse imaging, cells were incubated in an environment chamber (5% CO₂ and 37°C)

Schnepp et al.

with a consistent media flow (0.5 mL/minute). Glutamine was supplemented for a final concentration of 2 mmol/L. Cells were maintained in initial reduced media condition for 10 minutes prior to image acquisition. Time-lapse imaging was performed on a Nikon A1-R confocal microscope (ex:488 nm em:561 nm). ImageJ and custom MatLab codes were used to subtract background, determine fluorescent intensity, and generate pixel-by-pixel green-to-red ratio image for each time point. Fluorescence baseline value of each cell at the initial time point was defined as relative level 1.0.

***In vivo* animal experiments**

All animal experiments and terminal endpoints were carried out in accordance with approved protocols by Notre Dame Institutional Animal Care and Use Committee. Primary mammary fat pad (MFP) tumors were established by injection of 5×10^6 tumor cells orthotopically into the MFP of 12-week-old Rag1^{-/-} mice. Brain metastatic tumors were established by either intracarotid injection of tumor cells (2.5×10^5 cells in 0.1 mL of serum-free media) or intracranial injection (5×10^4 cells in 2 μ L of serum-free media). The endpoints of *in vivo* experiments are based on the presence of clinical signs of brain metastasis, including but not limited to, primary central nervous system disturbances, weight loss, and behavior abnormalities. Animals are culled after showing the above signs or 3 week after surgery. Eight hematoxylin and eosin (H&E)-stained sagittal sections through the left hemisphere of the brain were analyzed for the presence of metastatic lesions. Brain metastases incidence was quantified by identification of tumors from fluorescent images of total brain (A375SM) or by identification of tumors from H&E-stained sections (MDA-MB-231).

IHC and immunofluorescence staining

Standard IHC was performed as described previously (14). Immunofluorescence was performed following the standard protocol (Cell Signaling Technology). ImageJ was used for quantification of pixel-by-pixel intensity of staining.

Statistical analysis

For quantitative data with normal distribution, the Student *t* test was used for comparing two groups. All *P* values are two tailed. A difference with *P* < 0.05 (two sided) was considered statistically significant.

Results

Brain metastatic microenvironment induces a global metabolic transcriptome shift

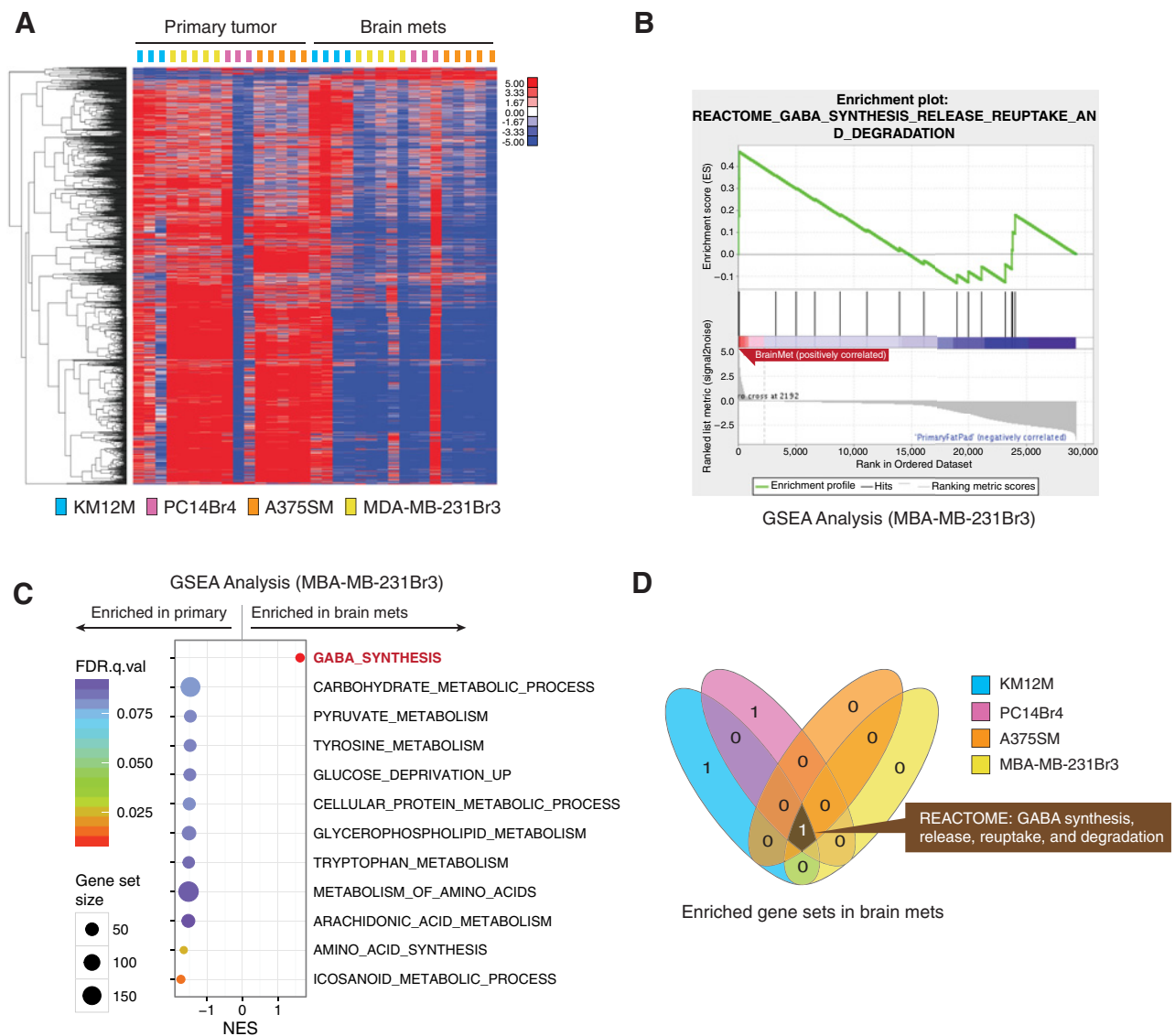
To examine the global influence of the brain metastatic microenvironment on cancer cell metabolism *in vivo*, we performed bioinformatics analysis focusing on curated metabolism-related genes using a publicly available cDNA microarray dataset (GSE19184), containing gene expression data generated from either primary xenograft tumors or brain metastases counterparts. This dataset represents major tumor types that metastasize to the brain, including lung (KM12M), colon (PC14Br4), melanoma (A375SM), and breast (MDA-MB-231Br3). Surprisingly, we observed a global downregulation of the majority of metabolism-related genes in brain metastatic tissues compared with respective primary tumors, regardless of their distinct primary tumor of origin (Fig. 1A). In contrast, only a small set of metabo-

lism-related genes were upregulated in brain metastases (Fig. 1A, top right), suggesting that brain metastases engage a specific metabolic program that is vital for sustaining their energy needs. We performed GSEA to further determine the functional implications of the tumor metabolic shift. Interestingly, despite the majority of metabolism-related gene sets were negatively enriched in the brain metastatic tumors, only one gene set (REACTOME: GABA synthesis, release, reuptake, and degradation) was significantly enriched in the brain metastatic tumors in all four cell lines (Fig. 1B–D, Supplementary Fig. S1; Supplementary Table S1). GABA is an inhibitory neurotransmitter primarily found in GABAergic neurons (25). In line with a recent clinical finding demonstrating GABA receptor upregulation in human HER2⁺ breast cancer brain metastases (16), enrichment of GABA signaling in brain metastatic tumor cells suggests that the metastatic tumor cells might adapt and shift to more neuronal-like signaling to thrive in the brain microenvironment. To mimic the brain microenvironment, we cocultured MDA-MB-231Br cells with primary brain glia cells and observed an increase in one GABA receptor isoform, GABRA1, compared with tumor cells alone (Supplementary Fig. S2A). Examining the "REACTOME: GABA synthesis, release, reuptake, and degradation" gene set further revealed glutamate decarboxylase 1 (GAD1) as among the only three significantly upregulated genes in brain metastases (Fig. 2A). GAD1 catalyzes the production of GABA from L-glutamic acid and is primarily found in the cytosol to provide an intracellular source of GABA for cell metabolism (26). As other cellular processes to catabolize glutamine (and glutamate) were downregulated (Supplementary Fig. S2B and S2C; Supplementary Table S2) in brain metastatic tumor cells, we reasoned that the GAD1-mediated GABA pathway could be the primary method for utilizing glutamine as an energy source in metastatic tumor cells.

To validate the observed increase of GAD1 in brain metastases from our bioinformatics analysis, we injected MDA-MB-231 parental cells (MDA-MB-231 here after), a non-brain-seeking triple-negative breast cancer cell line, into either the brain or mammary fat pad to model brain metastases and primary breast cancer. Using human-specific qRT-PCR primers, we detected a significant increase of GAD1 mRNA expression in the brain metastatic tumor compared with the primary tumors (Fig. 2B, *P* < 0.01). To model the different tissue microenvironments *in vitro*, we cocultured tumor cells with either Cav1^{-/-} fibroblast (CAF) cells or primary glia cells to model the primary cancer microenvironment or brain metastatic microenvironment, respectively (14, 27). Compared with CAF coculture, coculture with primary glia cells led to a significant increase of GAD1 mRNA expression in both MDA-MB-231 cells and A375SM cells (Fig. 2C, *P* < 0.01), which was associated with increased cell proliferation of tumor cells (Fig. 2D, left, *P* < 0.001). Importantly, the proliferative advantage imposed by glia coculture was completely abolished by inducible knockdown of GAD1 in tumor cells (Fig. 2D, right, *P* < 0.0005 and Supplementary Fig. S3, *P* < 0.0001). Together, these data demonstrate that the brain metastatic microenvironment alters the cancer cell metabolic transcriptome and induces upregulation of GAD1 mRNA expression, thereby facilitating tumor cell proliferation.

Brain microenvironment-induced downregulation of DNMT1 reactivates GAD1 expression

Epigenetic regulation has been implicated in the regulation of GAD1 gene expression under certain pathologic conditions,

**Figure 1.**

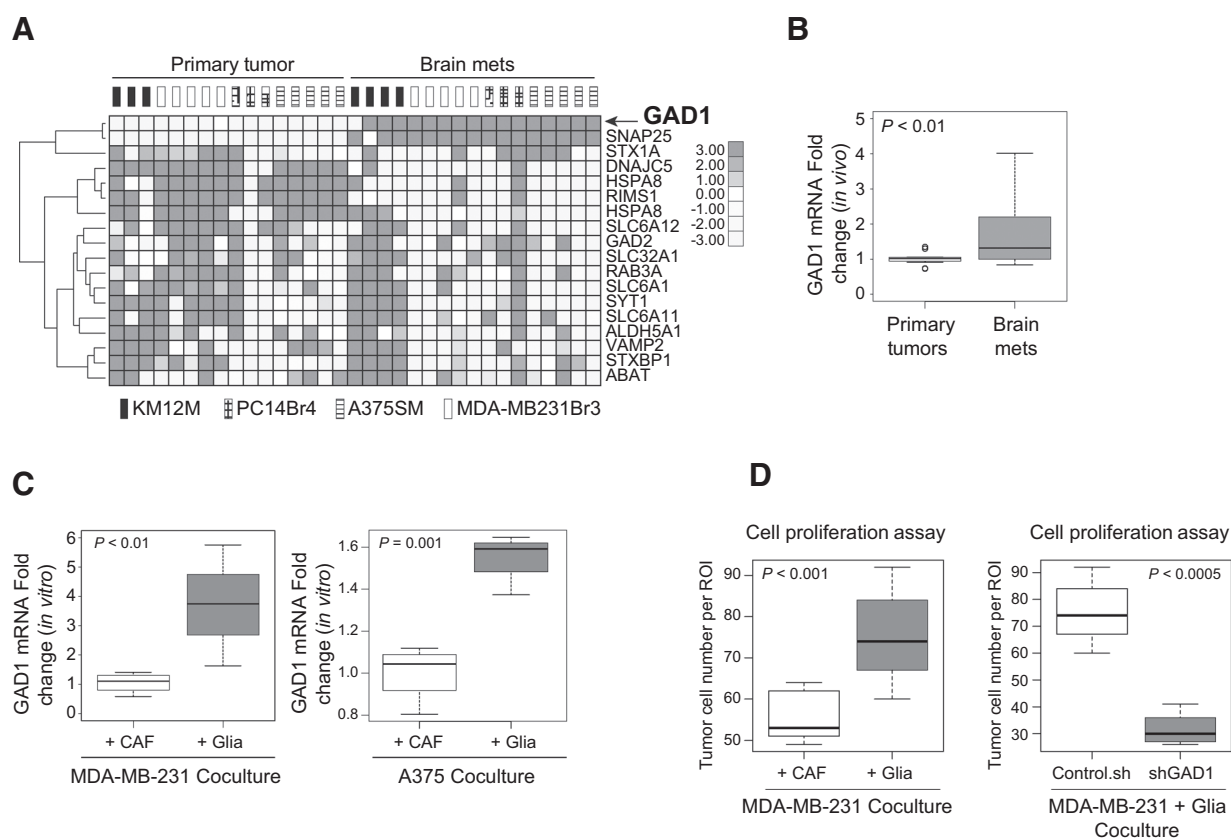
Metastatic microenvironment induces metabolic transcriptome shift. **A**, Heatmap of differentially expressed metabolic genes identified from bioinformatic analysis of GSE19184. **B**, GSEA result of gene sets enriched in either brain metastatic or primary tumor samples arising from MDA-MB-231Br3. **C**, Cleveland plot of top 10 gene sets enriched in either brain metastatic or primary tumor samples arising from MDA-MB-231Br3. **D**, Venn diagram of gene sets enriched in the brain metastatic samples arising from indicated cell lines.

such as schizophrenia (28). We examined the ENCODE data track of the GAD1 genomic locus (29) and found that CpG islands located on the GAD1 promoter are heavily methylated in differentiated cancer cell lines (K562, HeLa, and HepG2) while demethylated in human embryonic stem cells (hESC; Fig. 3A). This suggests a possible methylation-dependent regulation of GAD1 mRNA transcription (30). We first performed methylation-specific PCR (MSP) using human-specific primers to multiple CpG sites along the GAD1 promoter (Supplementary Fig. S4). Coculture with glia cells decreased GAD1 promoter methylation compared with coculture with CAFs (Fig. 3B). Bisulfate sequencing of CpG island 122 located in the GAD1 promoter further validated a decreased GAD1 promoter methylation under the glia cell coculture (Fig. 3C,

$P < 0.05$). Consistently, *in vivo* brain metastases exhibited a similar decrease in GAD1 promoter methylation compared with paired primary tumors (Fig. 3D).

As the primary enzyme regulating the propagation of DNA methylation (31), DNA (cytosine-5)-methyltransferase 1 (DNMT1) has been shown to regulate GAD1 through DNA methylation in multiple physiologic conditions (28). Interestingly, we observed a significant decrease of DNMT1 mRNA in brain metastatic tissue compared with paired primary tumors derived from A375SM and MDA-MB-231Br3 cells ($q < 0.005$ and $q < 0.001$, respectively) in our bioinformatics analysis of GSE19184 (Fig. 3E). Moreover, we detected a significant reduction of DNMT1 mRNA expression using independent, paired tumor sets (brain vs. primary; Fig. 3F, $P < 0.0001$) and cocultured

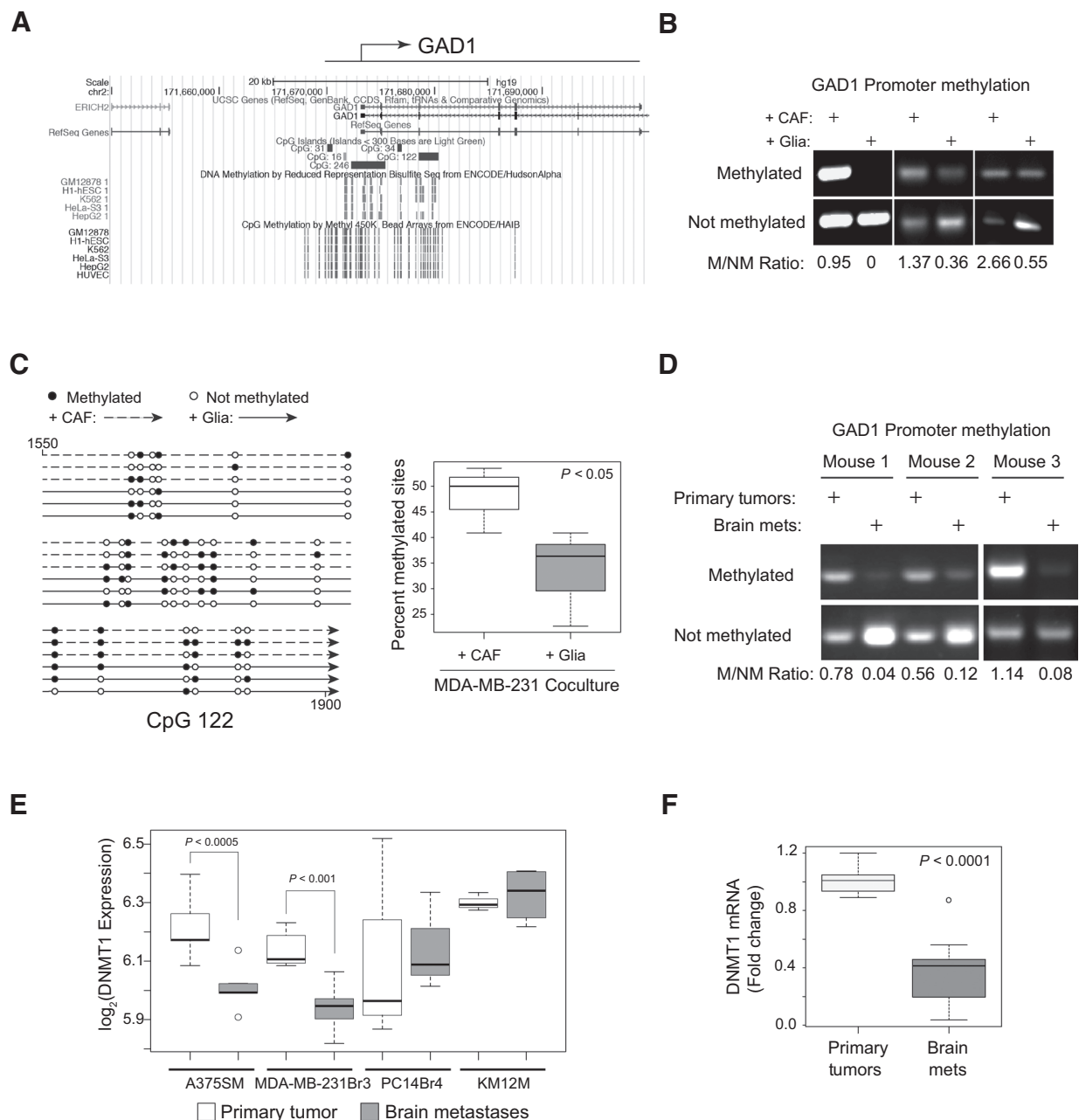
Schnepp et al.

**Figure 2.**

Brain microenvironment induces GAD1 upregulation. **A**, Heatmap of reactome. GABA synthesis, release, reuptake, and degradation gene set from bioinformatic analysis of GSE19184. **B**, qRT-PCR validation of GAD1 mRNA expression using tissue samples of either primary or brain metastatic tumors derived from MDA-MB-231. **C**, qRT-PCR of GAD1 mRNA expression of tumor cells after 48-hour coculture with either CAFs or glia cells; left, MDA-MB-231; right, A375SM. **D**, Left, cell proliferation assay of MDA-MB-231 after 48 hours of coculture with CAF or primary glia cells; right, cell proliferation assay of MDA-MB-231 with or without knockdown of GAD1 by transfection with either control shRNA or GAD1-targeting shRNA prior to coculture with primary glia cells for 48 hours with doxycycline-containing reduced media.

with glia, but not CAF cells, led to a prominent decrease in DNMT1 mRNA expression in both MDA-MB-231 and A375 cells (Fig. 4A, $P < 0.005$ and $P < 0.001$, respectively). Consistently, DNMT1 protein expression was also decreased in glia coculture (Supplementary Fig. S5A), while there are no evident changes in DNMT3A and DNMT3B mRNA and protein (Supplementary Fig. S5B–S5D). The above evidence suggests that the brain microenvironment induces demethylation of the GAD1 promoter, possibly through downregulation of DNMT1. To determine whether the altered DNMT1 expression in tumor cells induced by glia coculture requires direct cell-to-cell contact, we cultured tumor cells using conditioned media from either glia or CAF cells. Culture with glia-conditioned media, but not CAF-conditioned media, reduced DNMT1 mRNA expression (Fig. 4B, $P < 0.05$). Consistently, when we cultured tumor and stromal cells in a transwell system, we observed a similar decrease in DNMT1 expression (Supplementary Fig. S5E, gray boxes, $P < 0.005$) and a corresponding increase in GAD1 expression (Supplementary Fig. S5E, white boxes, $P < 0.005$), suggesting an unique glia-secretory factors influence DNMT1 gene expression in tumor cells. Next, we conducted an unbiased cytokine screen to identify the glia-secretory factor influencing the epigenetic regulation of GAD1 in tumor cells. We identified 74 differentially expressed

cytokines between conditioned media from glia cells or CAF cells (Fig. 4C, left, $P_{\text{adj}} < 0.1$) with 44 cytokines enriched in glia conditioned media (Fig. 4C, right, heatmap). We further performed network analysis using online NetworkAnalyst tools. We constructed densely connected modules and nodes based on the number of first-degree interactions. Interestingly, NetworkAnalyst revealed the cytokine clusterin as the top-ranked key nodes (centrality degree = 74, betweenness = 17,320.89; Fig. 4D; Supplementary Table S3) and is highly expressed in the glia conditioned media (Fig. 4E, left, $P < 0.05$). Clusterin is a glycoprotein increased in pathologic conditions that has been implicated in cancer and cellular adaptive responses to extracellular stresses, such as metabolic stress (32, 33). Direct treatment of clusterin dramatically reduced DNMT1 expression in tumor cells and resulted in GAD1 upregulation (Fig. 4E, right, white boxes, $P < 0.00001$) and a decrease in DNMT1 (Fig. 4E, right, gray boxes, $P < 0.00005$). To examine whether glia-derived clusterin is responsible for DNMT1 reduction in tumor cells, we conducted loss-of-function experiment by knocking down clusterin in glia cells prior to coculture. Knocking down glia clusterin mRNA expression (Fig. 4F, left, $P < 0.00001$) led to a decrease in GAD1 mRNA (Fig. 4F, right, white boxes, $P < 0.005$) and an increase in DNMT1 mRNA (Fig. 4F, right, gray boxes, $P < 0.005$) in the tumor

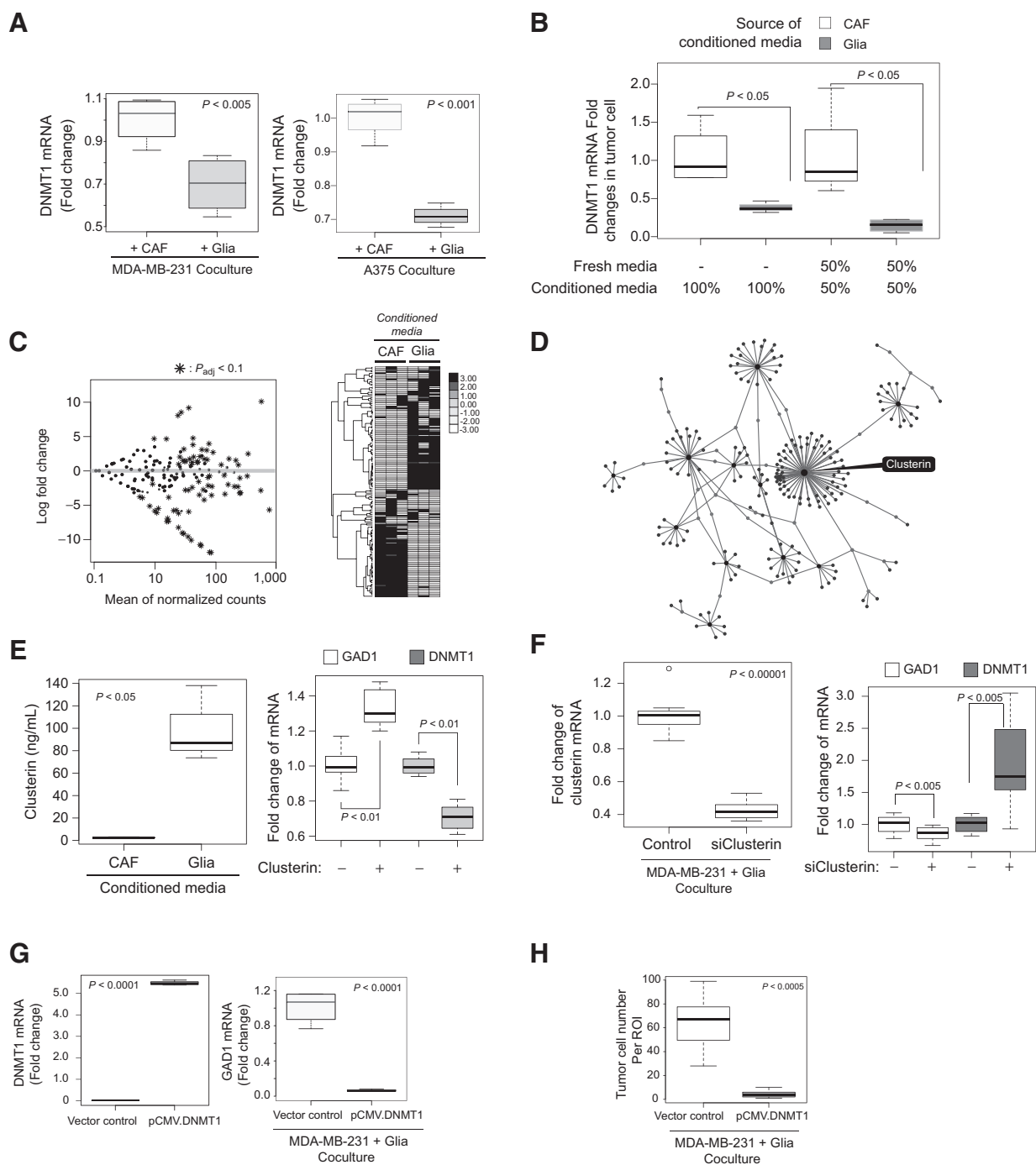
**Figure 3.**

Altered tumor cell GAD1 promoter methylation and DNMT1 expression induced by brain microenvironment. **A**, UCSC Genome Browser plot of ENCODE data track of CpG islands located around the GAD1 promoter. **B**, Promoter MSP assay detecting methylation status in human GAD1 promoter region *in vitro*. **C**, Left, bisulfite sequencing of CpG island 122 located in human GAD1 promoter region; right, percentage of methylated CpG sites in sequenced region. **D**, MSP assay detecting methylation status in the human GAD1 promoter region *in vivo*. **E**, Bioinformatics analysis of GSE19184 showing normalized DNMT1 probe intensity in primary tumors or brain metastases arising from indicated cell lines. **F**, qRT-PCR of DNMT1 mRNA levels in primary tumors or brain metastases arising from MDA-MB-231.

cells after 48-hour coculture. To determine whether the brain microenvironment–induced reduction of DNMT1 is required for increased GAD1, we overexpressed DNMT1 in tumor cells (Fig. 4G, left, $P < 0.0001$) resulting in blocking glia-induced GAD1 upregulation (Fig. 4G, right, $P < 0.0001$) and proliferative advantage (Fig. 4H, $P < 0.0005$). Finally, we targeted DNMT1 in tumor cells using an esiRNA (Supplementary Fig. S5F, left, $P <$

0.0001) resulting in increased GAD1 expression in tumor cells (Supplementary Fig. S5F, right, $P < 0.0001$). As both DNA methylation and histone modification status could potentially influence GAD1 expression, we further explored mRNA expression levels of histone modification enzymes in primary tumor and brain metastases microarray datasets. Surprisingly, we observed a general downregulation of a majority of these enzymes

Schnepp et al.

**Figure 4.**

Brain microenvironment-induced downregulation of DNMT1 reactivates GAD1 expression. **A**, qRT-PCR of DNMT1 mRNA expression after 48-hour coculture with either CAF or glia cells; left, MDA-MB-231; right, A375SM. **B**, qRT-PCR of DNMT1 mRNA expression of MDA-MB-231 cultured either with 100% conditioned media from either CAF or glia cells or 50% mix of conditioned media and fresh media. **C**, Cytokine screen of glia and CAF conditioned media; left, MA plot of log (mean expression of Glia/CAF) of 73 cytokines analyzed. *, differentially expressed cytokines ($P_{adj} < 0.1$). Right, heatmap of differentially expressed cytokines. **D**, Network analysis of differentially expressed cytokines. **E**, Impact of extracellular clusterin on DNMT1 and GAD1 expression. Left, cytokine expression profile of clusterin in conditioned media from CAFs or glia cells; right, qRT-PCR of GAD1 and DNMT1 mRNA expression in MDA-MB-231 cells treated with control or 200 ng of clusterin. **F**, qRT-PCR of GAD1 and DNMT1 mRNA expression in tumor cells genetic knockdown of glia-derived clusterin. Left, qRT-PCR of clusterin mRNA expression in glia cells; right, qRT-PCR of GAD1 and DNMT1 mRNA expression in MDA-MB-231 cells cocultured with control glia or siClusterin glia cells. **G**, qRT-PCR of mRNA levels in tumor cells after 48-hour coculture with primary glia cells. Prior to coculture, tumor cells were transfected with either vector control or DNMT1 overexpression plasmid for 24 hours. Left, DNMT1 mRNA expression; right, GAD1 mRNA expression under glia coculture. **H**, Proliferation of MDA-MB-231 cells after DNMT1 overexpression and coculture with glia cells for 48 hours.

(Supplementary Fig. S6A). Using pair primary and brain metastases *in vivo* tissue sample, we validated the downregulation of histone deacetylase 1 (HDAC1) mRNA brain metastasis tissues (Supplementary Fig. S6B, $P < 0.005$). Because of the generally low expression of HDACs, treating tumor cells with HDAC inhibitors did not result in a convincing restoration of GAD1 mRNA expression *in vitro* and *in vivo* (Supplementary Fig. S6C and S6D), suggesting the HDAC-mediated mechanism is unlikely to be the major contributor in GAD1 expression. Taken together, comprehensive epigenetic analysis suggests brain microenvironment-secreted clusterin downregulates DNMT1 in metastatic tumor cells, which subsequently leads to GAD1 upregulation.

GAD1 mediates a dynamic glutamine metabolic flux

Considering the role of GAD1 in regulating glutamine–GABA metabolism, we hypothesized that upregulation of GAD1 drives a metabolic shift toward glutamine-mediated metabolism. To visualize cellular metabolic events dynamically, we transfected MBA-MD-231 with a biosensor for real-time sensing of cytosolic NADH:NAD⁺ (Peredox; ref. 24). Increased GFP/RFP ratio (green/red ratio) as reported by time-lapse imaging of Peredox indicates NADH accumulation in the cytosol and a more oxidative cellular status (34). We cocultured tumor cells transfected with Peredox with either CAFs or primary glia cells under the precise control of media circulation, which allows us to alter extracellular glutamine concentrations and monitor intracellular NADH/NAD⁺ in real time (Fig. 5A). After an initial starvation period with glucose-free and glutamine-free media for 15 minutes (T0–T1), we introduced glutamine into the coculture (Supplementary Fig. S7A and S7B, T1). The glia cocultured tumor cells responded dramatically to the glutamine, displaying a sharp decrease in green/red fluorescence ratio, indicating increased consumption of NADH, whereas the CAF cocultured tumor cells expressed a stable fluorescence signal, indicating no change in the NADH/NAD⁺ ratio (Supplementary Fig. S7A and S7B, T1 to T2). Upon removing glutamine, all tumor cells, regardless of coculture condition, showed an increase in green/red fluorescence ratio (Supplementary Fig. S7A and S7B, T2 to T3). These data suggest that glia cocultured tumor cells have a greater response to extracellular glutamine due to the brain stromal cell-directed metabolic shift. When applying glucose-containing media instead of glutamine-high media, we observed no increase in green/red fluorescence ratio (Supplementary Fig. S7C, T1 to T2). This suggests that glia cells shift the tumor cells to respond primarily to glutamine greater than glucose, a metabolite found in greater level in the brain parenchyma (35). To further characterize intracellular signaling in response to glutamine, we stained for phosphorylated AMPK (Thr172)(p-AMPK), a sensor of cellular energy homeostasis (36), at different time points during the glutamine starvation–replenish cycle. Under coculture with CAFs, p-AMPK in tumor cells increases during the starvation period and remains unchanged during the subsequent high glutamine and starvation periods, whereas the p-AMPK fluctuates moderately in the tumor cells cocultured with glia (Supplementary Fig. S8A and S8B). This result suggests that glia facilitates the ability of tumor cells to overcome metabolic stresses imposed by nutrient starvation.

To visualize the metabolic flux regulated by GAD1 expression, we cocultured glia cells with tumor cells transfected with either GAD1 siRNA or a nonsilencing control siRNA (Supplementary Fig. S8C, left, $P < 0.01$). We observed an increase of the green/red ratio in all tumors cells during the initial starvation period (Fig. 5B

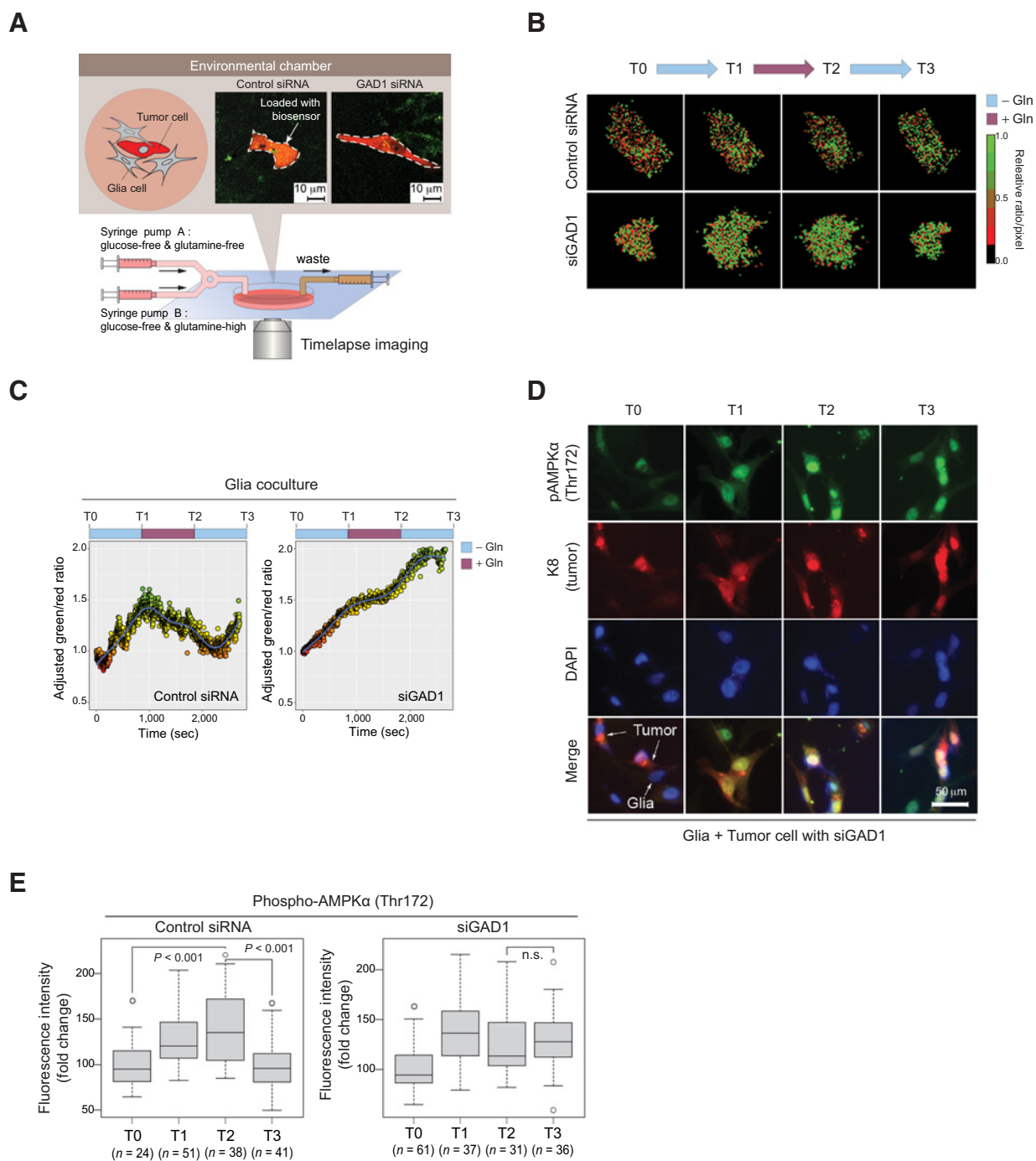
and C, T0–T1). Once glutamine was introduced into the media, tumor cells transfected with siGAD1 did not respond to glutamine (Fig. 5B, T1–T2). Real-time imaging revealed a continuous increase of the green/red ratio in siGAD1 cells, despite coculture with glia cells (Fig. 5C). However, in the control siRNA group, replenishing glutamine led to an immediate decrease of the green/red ratio (Fig. 5B and C, T1–T2). When glutamine was removed from the media, all of the tumor cells displayed an increased green/red ratio, suggesting a more oxidative cellular status (Fig. 5C, T2–T3). Furthermore, increased staining of p-AMPK in tumor cells cocultured with primary glia cells in response to glutamine starvation (T0–T1) suggested an increase in anabolic metabolic pathways (Fig. 5D and E; Supplementary Fig. S8C, right). Consistent with this cellular behavior, when glia-induced overexpression of GAD1 was inhibited with siGAD1, tumor cells failed to utilize glutamine replenishment (T1–T2), indicated by sustained staining of p-AMPK (Fig. 5E). Taken together, our data demonstrate that glia-induced GAD1 is the key cellular metabolism enzyme responsible for the dynamic glutamine utilization capability of tumor cells, following metabolic shifting at the brain metastatic microenvironment.

Repurposing vigabatrin as an anti-brain metastatic therapy

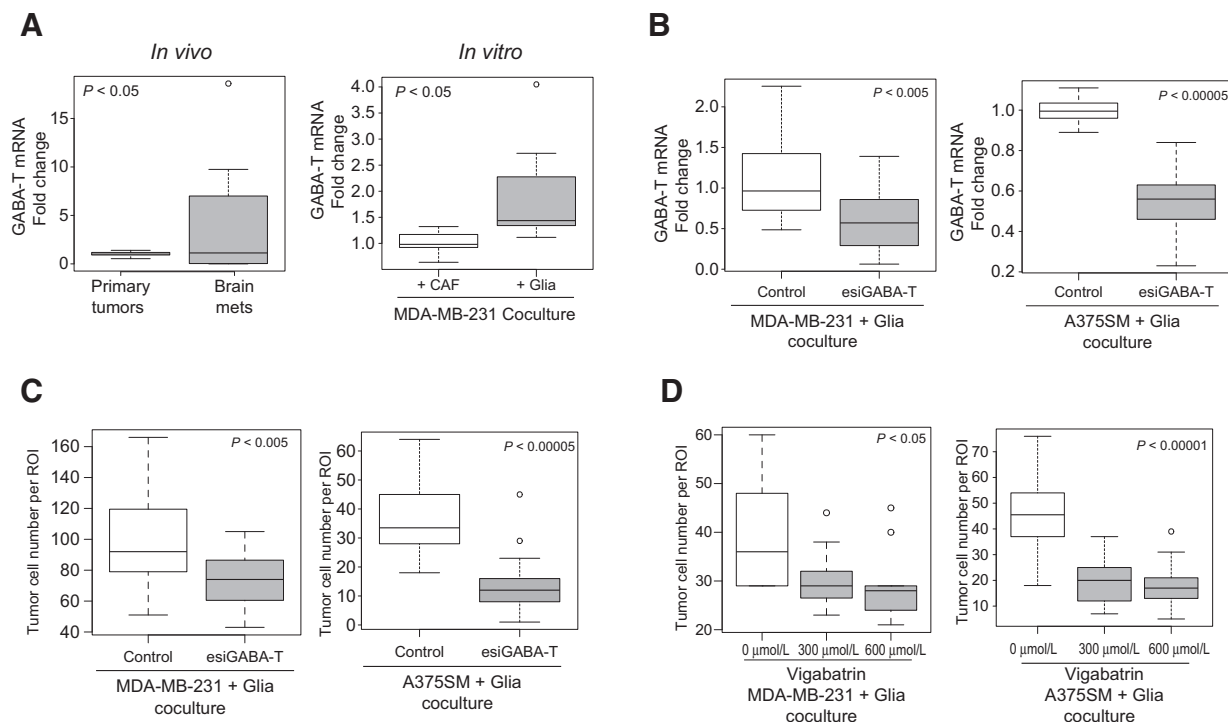
The reliance on brain microenvironment-dependent GAD1 upregulation to drive glutamine metabolism and cell proliferation represents a novel therapeutic opportunity for brain metastasis treatment. Modulation of GAD1-mediated GABA metabolism has been clinically exploited previously as an antiepileptic therapy (37, 38). One such drug, vigabatrin, targets GABA metabolism by inhibiting GABA transaminase (GABA-T), an enzyme directly downstream of GAD1. Vigabatrin thus functions to block GABA flux into the TCA cycle (39). Because of the essential role of GAD1-mediated GABA signaling in metastatic outgrowth, we hypothesize that vigabatrin could be repurposed to block tumor cell utilization of GABA as a metabolite, thereby decreasing metastatic outgrowth. Examination of GABA-T expression revealed an increase in both brain metastatic tumor samples (Fig. 6A, left, $P < 0.05$) and tumor cells cocultured with glia cells (Fig. 6A, right, $P < 0.05$), which is likely to be a result of downstream positive feedback in response to upregulated GAD1–GABA signaling. Knocking down GABA-T genetically (Fig. 6B, $P < 0.005$) did not alter the GAD1 expression (Supplementary Fig. S9A), but decreased glia-induced tumor cell proliferation in both the MDA-MB-231 (Fig. 6C, left, $P < 0.05$) and A375SM cell lines (Fig. 6C, right, $P < 0.00005$), suggesting GABA-T is a downstream signaling node responsible for GAD1's tumor-promoting function. Consistently, targeting GABA-T pharmacologically with vigabatrin resulted in a dose-dependent reduction in tumor cell proliferation under glia coculture (Fig. 6D, $P < 0.05$), without significant impacts on the migratory potential of the tumor cells (Supplementary Fig. S9B). Collectively, these data suggest that targeting GABA-T is a potentially viable brain metastasis therapy, which could block the proliferation potential of tumor cells in the brain microenvironment.

To explore the possibility of targeting the GAD1 metabolic pathway as anti-brain metastasis therapy *in vivo*, we induced shRNA expression after metastatic extravasation of tumor cells (7 days after intracarotid injection; Supplementary Fig. S9C). We observed a significant decrease in metastases with shGAD1 (GFP) compared with control shRNA cells (RFP) in both the A375SM

Schnepp et al.

**Figure 5.**

GAD1 mediates dynamic tumor glutamine metabolic flux. **A**, Schematic of experimental setup. **B**, Heatmaps of time course of changes in fluorescence ratio of Peredox biosensor throughout indicated time points. Prior to biosensor study, MDA-MB-231 cells were transfected with either control or GAD1 targeting siRNA for 24 hours and then cocultured with glia cells for another 48 hours. T0, 48-hour coculture in reduced media; T1, 15 minutes of incubation in glucose-free and glutamine-free media; T2, 15 minutes of incubation in glucose-free and 2 mmol/L glutamine media; T3, 15 minutes of incubation in glucose-free and glutamine-free media. **C**, Time course measurements of green/red fluorescence ratio of Peredox biosensor in MDA-MB-231. Tumor cells were transfected, cocultured, and treated as in **B**. **D**, Representative images of immunofluorescence staining of tumor cell's phosphorylated AMPK at Thr172 (pAMPK) and tumor-specific marker cytokeatin 8 (K8) at indicated time point after 48-hour coculture with glia cells following transfection with GAD1 targeting siRNA. Time-course experiments (T0–T3) were conducted as in **B**. **E**, Quantification of pAMPK fluorescence intensity in tumor cells from images in **D**.

**Figure 6.**

Suppression of metastatic tumor cell proliferation *in vitro* by targeting GABA-T. **A**, qRT-PCR of GABA-T mRNA expression. Left, primary tumor or brain metastatic samples arising from MDA-MB-231 cell line; right, MDA-MB-231 cells cocultured with either CAF or glias for 48 hours in reduced media. **B**, qRT-PCR of GABA-T after tumors were transfected with esiRNA targeting GABA-T or control and then cocultured with glias for 48 hours. Left, MDA-MB-231 cells; right, A375SM cells. **C**, Proliferation of tumor cells after transfection with esiRNA targeting GABA-T or control and then cocultured with glias for 48 hours. Left, MDA-MB-231 cells; right, A375SM cells. **D**, Proliferation of tumor cells after coculture with glias and treatment of vigabatrin, either control, 300 $\mu\text{mol/L}$, or 600 $\mu\text{mol/L}$. Left, MDA-MB-231 cells; right, A375SM cells.

(Fig. 7A, $P < 0.05$) and MDA-MB-231 models (Fig. 7B, $P < 0.00001$). These data suggest ablation of brain microenvironment-induced metabolic shifting to GAD1-GABA signaling is critical for successful brain metastatic outgrowth. As we have demonstrated targeting GABA-T effectively suppressed tumor cell proliferation, we treated metastasis-bearing mice with either 4 mg/kg (clinically recommended dosage for antiseizure treatment) or 7 mg/kg vigabatrin daily intraperitoneally. As expected, inhibiting GABA-T led to an evident accumulation of GABA in tumor cells *in vitro* (Supplementary Fig. S9D, $P = 0.0218$). After a 7-day course of 4 mg/kg daily vigabatrin, the metastatic burden is dramatically decreased compared with vehicle-treated mice (Fig. 7C). There were no detectable morphologic differences in residual brain metastases (Fig. 7D, left, H&E staining). We observed a dose-dependent decrease in the number of metastases (Fig. 7D, right, $P < 0.01$), which is associated with a decrease in Ki-67⁺ tumor cells (Fig. 7E, $P < 0.05$). Together, these data suggest that blocking GABA flux into the TCA cycle, either through genetic depletion of GAD1 or pharmacologic treatment with vigabatrin, significantly suppressed aggressive metastatic outgrowth in the brain.

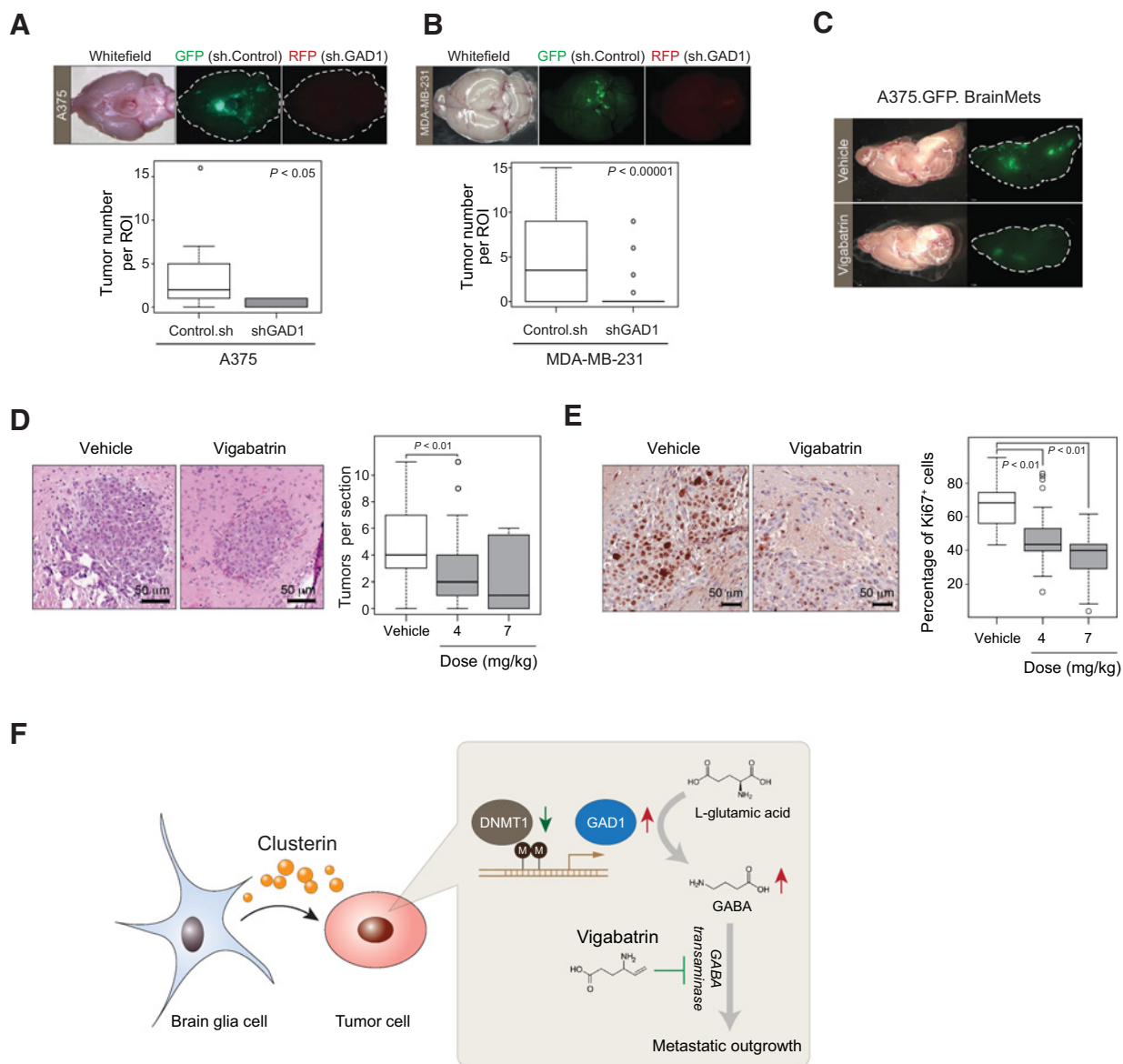
Discussion

One of the emerging hallmarks of cancer is deregulated metabolism (40). Yet, the dynamic nature of metabolic repro-

gramming in response to metastatic microenvironments, such as the brain, has not been fully characterized. During the metastatic process, highly metastatic "seeds" from the primary tumor microenvironment experience a series of metabolic stresses and ultimately settle in an exotic metastatic microenvironment: the brain, an organ that maintains a unique metabolism equilibrium (7, 11). Our study illustrates the striking metabolic plasticity of metastatic tumor cells. To take the greatest advantage of available metabolites, metastatic tumor cells, regardless of their primary tumor of origin, metabolically adapt to the brain microenvironment by engaging the GAD1-GABA synthesis pathway to facilitate metastatic outgrowth (Fig. 7F). In accordance with the previous observation of upregulated GABA receptors in brain metastatic tumors derived from HER2⁺ breast cancer patients (16), our study significantly expands the relevance of this finding by revealing a mechanism of epigenetic upregulation of the key GABA synthesis enzyme GAD1 in multiple tumor types that drives an increased intracellular GABA metabolism. Our study also highlighted a clinically targetable mechanism for brain metastasis treatment (Fig. 7F).

The data from this study shed light on the emerging concept of metastatic cooption. Cooption is essential to many biological ecosystems, including disease conditions (41). Conceivably, metastasis, as a well-known multistep, tissue context-dependent biological process, requires a series of cooptions to facilitate

Schnepp et al.

**Figure 7.**

GAD1-mediated glutamine metabolism enables brain metastatic outgrowth. **A**, Top, representative images of A375SM brain metastatic tumors arising from 1:1 mix of tumor cells expressing either control (labeled with GFP) or GAD1-targeted shRNA (labeled with RFP); bottom, quantification of metastatic incidence. **B**, Top, representative images of MDA-MB-231 brain metastatic tumors with/without GAD1 knockdown; bottom, quantification of metastatic incidence. **C**, Representative images of brain metastatic tumors arising from A375SM cells after treating with vehicle control or vigabatrin (4 mg/kg) for 7 days, beginning at 7 days postinjection. **D**, Reduction of metastatic tumor lesions by vigabatrin. Left, representative images of metastatic tumors treated with either control or vigabatrin (4 mg/kg); right, quantification of stained tumors per section. **E**, Ki-67 IHC staining of tumors arising in mice treated with either vehicle control or vigabatrin (4 mg/kg); left, representative images of Ki-67 staining; right, quantification of Ki-67⁺ tumor cells per region of interest. **F**, Proposed model of brain microenvironment-induced tumor cell metabolic shifting via clusterin-mediated epigenetic upregulation of GAD1, which contributes to brain metastatic outgrowth.

ultimate metastasis success. Indeed, during early metastatic colonization, blood vessel cooption has been observed and is believed to be essential for metastasis outgrowth (42). In our study, we demonstrated an indispensable form of metabolic cooption, in which metastatic tumor cells mimic astrocyte–neuron cooperation, by adopting a similar metabolic phenotype. Cooperation between astrocytes and neurons enables metabolic compartmentalization and precise metabolite regulation between

astrocytes and neurons (7, 11). In the normal brain tissue, glutamine metabolism primarily occurs in the astrocytes yet GABA synthesis occurs predominately in GABAergic neurons (7, 11). Reminiscent of neurologic disorders (28), metastatic tumor cells exhibit methylation-dependent upregulation of GAD1, which is a marker of GABAergic neurons (43), and decrease of other glutamine catabolic processes (Fig. 2A–C; Supplementary Fig. S2B and S2C). The altered metabolic phenotype,

characterized by neuronal-like expression of the GAD1–GABA pathway, favors GABA synthesis in tumor cells and subsequently enables tumor cells to thrive in the glutamine-rich brain metastatic microenvironment. Because of the overarching role of DNMT1 in the regulation of DNA methylation, it is reasonable to envision that a collective transcriptome shifting of a number of DNMT1-regulated genes orchestrates the highly dynamic brain metastasis process. Further study would be necessary to functionally reveal and validate other significant contributors in the brain metastasis context.

Furthermore, our data lay the groundwork for clinically translatable targeted therapies for patients suffering with brain metastases. Currently, brain metastasis patients have limited treatment options, mainly surgery or radiotherapy (44). One of the major obstacles in developing therapies for brain metastasis is the presence of the BBB. The BBB acts as the barrier to prevent molecules from the vascular system from reaching the brain parenchyma (45). Most chemotherapeutic drugs fail to cross the BBB, making the brain a sanctuary organ for cancer cells (46). Fortunately, in developing treatments for mental disorders, there is a repertoire of clinical neurologic drugs that have been proven to cross the BBB. Mechanistically, our data illustrate that brain metastatic tumor cells upregulate a shared common signaling node, GAD1-GABA, with clinical seizures, which has been successfully targeted by the neurologic drug, vigabatrin (38). Vigabatrin acts a suicide inhibitor of the enzyme directly downstream of GAD1, GABA transaminase (GABA-T), leading to an accumulation of GABA. For patients suffering from epilepsy, the increased pool of GABA results in a decrease in epileptic seizures (39). At the same time, inhibiting GABA-T also prevents GABA flux into the TCA cycle in tumor cells, suggesting that repurposing this neurologic drug for brain metastasis may inhibit tumor GABA metabolism. One previous study suggested that treatment of HER2⁺ breast cancer cells with vigabatrin decreases proliferation *in vitro* (16). Our study further demonstrated vigabatrin as a highly promising brain metastasis therapy using an *in vivo* model of brain metastases (Fig. 7C–E). Expanding the applicability of these findings for additional brain metastases that arise from other cancer is of interest for further study. Extravagated tumor cells lose their metastatic outgrowth capability in brain when vigabatrin is used to block GABA flux, decreasing both metastasis number and proliferation index (Fig. 7C–E). It is important to note that brain tumor patients frequently experience seizures due to the deprivation of inhibitory neurotransmitter GABA around the tumor site (47). This suggests that in addition to treating brain metastases, vigabatrin might bring an additional benefit of stabilizing tumor-induced seizures, which is of interest for future preclinical and

clinical study. Collectively, our study provides critical preclinical mechanistic evidence to support future clinical repurposing of FDA-approved GABA pathway targeting vigabatrin for brain metastatic patients.

In summary, our data demonstrate brain metastatic tumor cells adapt to the brain microenvironment by increasing GABA synthesis mediated by methylation-dependent upregulation of GAD1. The dependence of brain metastatic cells on GAD1 and GABA reveals novel mechanistic insights into brain metastasis progression and, more importantly, provides intriguing rationale for repurposing neurologic drugs as novel brain metastasis treatments.

Disclosure of Potential Conflicts of Interest

No potential conflicts of interest were disclosed.

Authors' Contributions

Conception and design: P.M. Schnepf, S. Zhang

Development of methodology: P.M. Schnepf, S. Zhang

Acquisition of data (provided animals, acquired and managed patients, provided facilities, etc.): P.M. Schnepf, D.D. Lee, I.H. Guldner, E.N. Howe, B. Palakurthi, K.E. Eckert, T.A. Toni, S. Zhang

Analysis and interpretation of data (e.g., statistical analysis, biostatistics, computational analysis): P.M. Schnepf, D.D. Lee, E.N. Howe, B. Palakurthi, S. Zhang

Writing, review, and/or revision of the manuscript: P.M. Schnepf, I.H. Guldner, E.N. Howe, S. Zhang

Administrative, technical, or material support (i.e., reporting or organizing data, constructing databases): P.M. Schnepf, T.K. O'Tighearnigh, T.A. Toni, B.L. Ashfeld, S. Zhang

Study supervision: S. Zhang

Acknowledgments

We thank Notre Dame Integrated Imaging Facility for its technical support.

Grant Support

This work was partially supported by Department of Defense W81XWH-15-1-0021 (S. Zhang), NIH 1R01CA194697-01 (S. Zhang), Walther Cancer Foundation Advancing Basic Cancer Research Grant II (S. Zhang), Indiana CTISI core pilot fund (S. Zhang). P.M. Schnepf was funded through a Walther Cancer Foundation ENSCCII Pre-doctoral Fellowship. E.N. Howe was supported by NIH/NCATS institutional post-doctoral fellowship (Indiana CTISI TL1TR001107). T.A. Toni was supported by Summer Undergraduate Research Fellowship (NSF CAREER CHE-1056242).

The costs of publication of this article were defrayed in part by the payment of page charges. This article must therefore be hereby marked *advertisement* in accordance with 18 U.S.C. Section 1734 solely to indicate this fact.

Received August 22, 2016; revised September 19, 2016; accepted April 3, 2017; published OnlineFirst April 11, 2017.

References

- Fidler IJ. The pathogenesis of cancer metastasis: the "seed and soil" hypothesis revisited. *Nat Rev Cancer* 2003;3:453–8.
- Hanahan D, Weinberg RA. Hallmarks of cancer: the next generation. *Cell* 2011;144:646–74.
- Massagué J, Obenauf AC. Metastatic colonization by circulating tumour cells. *Nature* 2016;529:298–306.
- Nieman KM, Kenny HA, Penicka CV, Ladanyi A, Buell-Gutbrod R, Zillhardt MR, et al. Adipocytes promote ovarian cancer metastasis and provide energy for rapid tumor growth. *Nat Med* 2011;17:1498–503.
- Loo JM, Scherl A, Nguyen A, Man FY, Weinberg E, Zeng Z, et al. Extracellular metabolic energetics can promote cancer progression. *Cell* 2015;160:393–406.
- Chen EI, Hewel J, Krueger JS, Tiraby C, Weber MR, Kralli A, et al. Adaptation of energy metabolism in breast cancer brain metastases. *Cancer Res* 2007;67:1472–86.
- Cahoy JD, Emery B, Kaushal A, Foo LC, Zamanian JL, Christopherson KS, et al. A transcriptome database for astrocytes, neurons, and oligodendrocytes: a new resource for understanding brain development and function. *J Neurosci* 2008;28:264–78.

Schnepp et al.

8. Chowdhury GMI, Patel AB, Mason GF, Rothman DL, Behar KL. Glutamate and GABAergic neurotransmitter cycling and energy metabolism in rat cerebral cortex during postnatal development. *J Cereb Blood Flow Metab* 2007;27:1895–907.
9. Çakır T, Alsan S, Saybaşı H, Aktın A, Ülgen KÖ. Reconstruction and flux analysis of coupling between metabolic pathways of astrocytes and neurons: application to cerebral hypoxia. *Theor Biol Med Model* 2007;4:48.
10. Shank RP, Campbell GLM. α -Ketoglutarate and malate uptake and metabolism by synaptosomes: further evidence for an astrocyte-to-neuron metabolic shuttle. *J Neurochem* 1984;42:1153–61.
11. Bélanger M, Allaman I, Magistretti PJ. Brain energy metabolism: focus on astrocyte-neuron metabolic cooperation. *Cell Metab* 2011;14:724–38.
12. Magistretti PJ. Role of glutamate in neuron-glia metabolic coupling. *Am J Clin Nutr* 2009;90:875S–80S.
13. Magistretti PJ, Pellerin L. Astrocytes couple synaptic activity to glucose utilization in the brain. *Physiology* 1999;14:177–82.
14. Zhang L, Zhang S, Yao J, Lowery FJ, Zhang Q, Huang W-C, et al. Microenvironment-induced PTEN loss by exosomal microRNA primes brain metastasis outgrowth. *Nature* 2015;527:100–4.
15. Chen Q, Boire A, Jin X, Valiente M, Er EE, Lopez-Soto A, et al. Carcinoma-astrocyte gap junctions promote brain metastasis by cGAMP transfer. *Nature* 2016;533:493–8.
16. Neman J, Termini J, Wilczynski S, Vaidehi N, Choy C, Kowolik CM, et al. Human breast cancer metastases to the brain display GABAergic properties in the neural niche. *Proc Natl Acad Sci U S A* 2014;111:984–9.
17. Park ES, Kim SJ, Kim SW, Yoon S-L, Leem S-H, Kim S-B, et al. Cross-species hybridization of microarrays for studying tumor transcriptome of brain metastasis. *Proc Natl Acad Sci U S A* 2011;108:17456–61.
18. Mecha M, Inigo PM, Mestre L, Hernangomez M, Borrell J, Guaza C. An easy and fast way to obtain a high number of glia cells from rat cerebral tissue: A beginners approach. *Protoc Exchange* 2011.doi:10.1038/protex.2011.218.
19. Subramanian A, Tamayo P, Mootha VK, Mukherjee S, Ebert BL, Gillette MA, et al. Gene set enrichment analysis: A knowledge-based approach for interpreting genome-wide expression profiles. *Proc Natl Acad Sci U S A* 2005;102:15545–50.
20. Reich M, Liefeld T, Gould J, Lerner J, Tamayo P, Mesirov JP. GenePattern 2.0. *Nat Genet* 2006;38:500–1.
21. Xia J, Benner MJ, Hancock REW. NetworkAnalyst - integrative approaches for protein-protein interaction network analysis and visual exploration. *Nucleic Acids Res* 2014;42:W167–74.
22. Xia J, Gill EE, Hancock REW. NetworkAnalyst for statistical, visual and network-based meta-analysis of gene expression data. *Nat Protoc* 2015;10:823–44.
23. Li L-C, Dahiya R. MethPrimer: designing primers for methylation PCRs. *Bioinformatics* 2002;18:1427–31.
24. Hung YP, Albeck JG, Tantama M, Yellen G. Imaging cytosolic NADH-NAD⁺ redox state with a genetically encoded fluorescent biosensor. *Cell Metab* 2011;14:545–54.
25. Chebib M, Johnston GAR. The "abc" of gaba receptors: a brief review. *Clin Exp Pharmacol Physiol* 1999;26:937–40.
26. Pinal CS, Tobin AJ. Uniqueness and redundancy in GABA production. *Perspect Dev Neurobiol* 1998;5:109–18.
27. Sotgia F, Galdo FD, Casimiro MC, Bonuccelli G, Mercier I, Whitaker-Menezes D, et al. Caveolin-1^{-/-} null mammary stromal fibroblasts share characteristics with human breast cancer-associated fibroblasts. *Am J Pathol* 2009;174:746–61.
28. Dong E, Ruzicka WB, Grayson DR, Guidotti A. DNA-methyltransferase1 (DNMT1) binding to CpG rich GABAergic and BDNF promoters is increased in the brain of schizophrenia and bipolar disorder patients. *Schizophr Res* 2015;167:35–41.
29. ENCODE Project Consortium. An integrated encyclopedia of DNA elements in the human genome. *Nature* 2012;489:57–74.
30. Chen Y, Dong E, Grayson DR. Analysis of the GAD1 promoter: Trans-acting factors and DNA methylation converge on the 5' untranslated region. *Neuropharmacology* 2011;60:1075–87.
31. Jones PA. Functions of DNA methylation: islands, start sites, gene bodies and beyond. *Nat Rev Genet* 2012;13:484–92.
32. Athanas KM, Mauney SL, Woo T-UW. Increased extracellular clusterin in the prefrontal cortex in schizophrenia. *Schizophr Res* 2015;169:381–5.
33. Pucci S, Mazzarelli P, Nucci C, Ricci F, Spagnoli LG. CLU "in and out": looking for a link. *Adv Cancer Res* 2009;105:93–113.
34. Teodoro JS, Rolo AP, Palmeira CM. The NAD ratio redox paradox: why does too much reductive power cause oxidative stress? *Toxicol Mech Methods* 2013;23:297–302.
35. Yudkoff M, Nissim I, Daikhin Y, Lin Z-P, Nelson D, Pleasure D, et al. Brain glutamate metabolism: neuronal-astroglia relationships. *Dev Neurosci* 1993;15:343–50.
36. Hardie DG. AMP-activated protein kinase—an energy sensor that regulates all aspects of cell function. *Genes Dev* 2011;25:1895–908.
37. Sugino K, Hempel CM, Miller MN, Hattox AM, Shapiro P, Wu C, et al. Molecular taxonomy of major neuronal classes in the adult mouse fore-brain. *Nat Neurosci* 2006;9:99–107.
38. Grant SM, Heel RC. Vigabatrin. *Drugs* 2012;41:889–926.
39. Tolman JA, Faulkner MA. Vigabatrin: a comprehensive review of drug properties including clinical updates following recent FDA approval. *Expert Opin Pharmacother* 2009;10:3077–89.
40. Pavlova NN, Thompson CB. The emerging hallmarks of cancer metabolism. *Cell Metab* 2016;23:27–47.
41. True JR, Carroll SB. Gene co-option in physiological and morphological evolution. *Annu Rev Cell Dev Biol* 2002;18:53–80.
42. Yancopoulos GD, Davis S, Gale NW, Rudge JS, Wiegand SJ, Holash J. Vascular-specific growth factors and blood vessel formation. *Nature* 2000;407:242–8.
43. Kodama T, Guerrero S, Shin M, Moghadam S, Faulstich M, Lac S du. Neuronal classification and marker gene identification via single-cell expression profiling of brainstem vestibular neurons subserving cerebellar learning. *J Neurosci* 2012;32:7819–31.
44. Langer CJ, Mehta MP. Current management of brain metastases, with a focus on systemic options. *J Clin Oncol* 2005;23:6207–19.
45. Abbott NJ, Rönnbäck L, Hansson E. Astrocyte-endothelial interactions at the blood-brain barrier. *Nat Rev Neurosci* 2006;7:41–53.
46. Steeg PS. Targeting metastasis. *Nat Rev Cancer* 2016;16:201–18.
47. Schaller B, Rüegg SJ. Brain tumor and seizures: pathophysiology and its implications for treatment revisited. *Epilepsia* 2003;44:1223–32.

Cancer Research

The Journal of Cancer Research (1916–1930) | The American Journal of Cancer (1931–1940)

GAD1 Upregulation Programs Aggressive Features of Cancer Cell Metabolism in the Brain Metastatic Microenvironment

Patricia M. Schnepf, Dennis D. Lee, Ian H. Guldner, et al.

Cancer Res 2017;77:2844-2856. Published OnlineFirst April 11, 2017.

Updated version Access the most recent version of this article at:
doi:[10.1158/0008-5472.CAN-16-2289](https://doi.org/10.1158/0008-5472.CAN-16-2289)

Supplementary Material Access the most recent supplemental material at:
<http://cancerres.aacrjournals.org/content/suppl/2017/04/11/0008-5472.CAN-16-2289.DC1>

Cited articles This article cites 46 articles, 9 of which you can access for free at:
<http://cancerres.aacrjournals.org/content/77/11/2844.full#ref-list-1>

E-mail alerts [Sign up to receive free email-alerts](#) related to this article or journal.

Reprints and Subscriptions To order reprints of this article or to subscribe to the journal, contact the AACR Publications Department at pubs@aacr.org.

Permissions To request permission to re-use all or part of this article, use this link
<http://cancerres.aacrjournals.org/content/77/11/2844>.
Click on "Request Permissions" which will take you to the Copyright Clearance Center's (CCC) Rightslink site.